

REPORT DOCUMENTATION PAGE

AFRL-SR-BL-TR-00-

Public reporting burden for this collection of information is estimated to average 1 hour per response, including gathering and maintaining the data needed, and completing and reviewing the collection of information, including suggestions for reducing this burden, to Washington Headquarters Services, Attention: Office of Management and Budget, Davis Highway, Suite 1204, Arlington, VA 22202-4302, and to the Office of Management and Budget.

a sources,
ect of this
Jefferson
13

1. AGENCY USE ONLY /Leave blank/		2. REPORT DATE	3. R	Final Report: 1 September 96 To 30 November 99 <i>0514</i>
4. TITLE AND SUBTITLE MODELING OF AN ARCJET PLUME FOR THIN FILM SYNTHESIS		5. FUNDING NUMBERS F49620-96-1-0210		
6. AUTHOR(S) Iain D. Boyd				
7. PERFORMING ORGANIZATION NAME(S) AND ADDRESS(ES) SCHOOL OF MECHANICAL AND AEROSPACE ENGINEERING Cornell University 246 Upson Hall Ithaca, NY 14853		8. PERFORMING ORGANIZATION REPORT NUMBER		
9. SPONSORING/MONITORING AGENCY NAME(S) AND ADDRESS(ES) AIR FORCE OFFICE OF SCIENTIFIC RESEARCH 801 N. Randolph St. Arlington VA 22203-1977		10. SPONSORING/MONITORING AGENCY REPORT NUMBER		
11. SUPPLEMENTARY NOTES				
12a. DISTRIBUTION AVAILABILITY STATEMENT Unlimited		12b. DISTRIBUTION CODE U,L		
13. ABSTRACT (Maximum 200 words) This final report summarizes the research carried out on the development of numerical approaches for simulating the plumes of electric propulsion devices. In Appendix I, we describe the development of a particle based Monte Carlo approach for simulating the plumes and impingement of chemical propulsion systems, in Appendix II, we describe a plume model for an electric propulsion device (a Hall thruster). The research performed in this grant has led to significant advances in the capabilities for modeling these plume flows.				
14. SUBJECT TERMS THREE DIMENSIONAL MONTE CARLO SIMULATIONS OF PLUME IMPINGEMENT		15. NUMBER OF PAGES 136		
		16. PRICE CODE		
17. SECURITY CLASSIFICATION OF REPORT	18. SECURITY CLASSIFICATION OF THIS PAGE	19. SECURITY CLASSIFICATION OF ABSTRACT	20. LIMITATION OF ABSTRACT	

FINAL TECHNICAL REPORT

05 SEP 2000

For research supported by
DOD/AFOSR AASERT Award F49620-96-1-0210

for the period 09/01/96 to 11/30/99

MODELING OF AN ARCJET PLUME FOR THIN FILM SYNTHESIS

prepared by

Iain D. Boyd ⁽¹⁾

School of Mechanical and Aerospace Engineering
Cornell University,
246 Upson Hall
Ithaca, NY 14853.

Work supported by
Air Force Office of Scientific Research

Grant Monitored By
Dr. Mitat A. Birkan

August 2000

(1) Principal Investigator

20001016 026

Table of Contents

	Page
Abstract	3
Overview	4
I. Three Dimensional Monte Carlo Simulations Of Plume Impingement	
II. Particle Simulations of a Hall Thruster Plume	

Abstract

This final report summarizes the research carried out on the development of numerical approaches for simulating the plumes of electric propulsion devices. In Appendix I, we describe the development of a particle-based Monte Carlo approach for simulating the plumes and impingement of chemical propulsion systems. In Appendix II, we describe a plume model for an electric propulsion device (a Hall thruster). The research performed in this grant has led to significant advances in the capabilities for modeling these plume flows.

Overview

The original premise of the proposed research was to develop a computer model for the plume of a particular spacecraft propulsion system (the arcjet) and to use the model to simulate synthesis of thin films. Early in the project, with the concurrence of the technical monitor, it was decided to concentrate on modeling the plume rather than the film synthesis processes. In addition, it was decided to focus not on arcjets but on the plumes of various chemical and electric propulsion devices.

The plumes of spacecraft propulsion systems are of interest because of their potential deleterious effects on the host spacecraft. Before undertaking the present research, plume models of spacecraft propulsion systems were not well advanced. Simple, two-dimensional models existed for chemical rockets and semi-empirical models existed for Hall thrusters. The research performed under this grant significantly advanced the modeling capabilities for both these types of rocket engines.

In terms of simulating the plumes of chemical rockets, the main activity involved the development of a three-dimensional, fully parallelized code employing the direct simulation Monte Carlo method (DSMC). The code was successfully verified against experimental data taken at DLR, Germany, for the three-dimensional impingement of a small rocket plume on a flat plate. The DSMC code was then applied to model impingement of a Primex hydrazine rocket plume on a typical spacecraft geometry. This work was published in the Journal of Thermophysics and Heat Transfer and the paper is included as Appendix I.

A second investigation involved the development of a computer code for simulating the plumes of Hall thrusters which are an important form of electric propulsion. In this case, a combination of the DSMC and Particle In Cell (PIC) techniques was employed. The computer code was again parallelized. The model was applied to the SPT-100 Hall thruster and its physical accuracy assessed through direct comparison with several different experimental data sets. This work was published in the Journal of Spacecraft and Rockets and the paper is included as Appendix II.

The research performed under this grant contributed significantly to two doctoral theses. One of the graduating students (Keith Kannenberg) now works at Lockheed Martin on spacecraft contamination, and the other (Doug VanGilder) works at Edwards AFB on the DSMC technique. Therefore, both the research and educational goals of the AASERT program have been successfully achieved.

Three-Dimensional Monte Carlo Simulations of Plume Impingement

Keith C. Kannenberg* and Iain D. Boyd†
Cornell University, Ithaca, New York 14853-7501

Three-dimensional plume impingement flows are simulated using the direct simulation Monte Carlo (DSMC) technique. Two impingement problems are computed. The impact of a jet of nitrogen on an inclined flat plate is considered. Good agreement is found between surface quantities calculated by DSMC and experimental data. A free molecular model of the plume is shown to provide reasonable estimates of impingement quantities. The plume of a hydrazine control thruster firing in a model satellite configuration is simulated. Surface quantities and net impingement effects are calculated. Free molecular analysis provides less accurate modeling of a multispecies flow with boundary-layer effects.

Nomenclature

A_p	= plume constant
C	= boundary-layer plume constant
C_p	= specific heat at constant pressure
p	= impingement pressure
q	= heat flux
R_E	= nozzle exit radius
r^*	= throat radius
T_w	= surface temperature
T_0, p_0	= stagnation temperature, pressure
U, ρ	= plume velocity, density
α	= local angle of incidence
γ	= ratio of specific heats
δ_E	= boundary-layer thickness at exit
η	= net parallel efficiency
θ_{lim}	= maximum inviscid turning angle
θ_0	= boundary-layer streamline angle
ρ^*	= throat density
σ	= accommodation coefficient
τ	= shear stress

Introduction

SPACECRAFT in orbit require propulsion systems for various functions such as attitude control and stationkeeping. Low-thrust rockets are often employed to meet these requirements. The gas plume that is produced during a thruster firing may impinge on spacecraft surfaces. Impingement can have a number of undesirable effects such as the production of additional forces and torques, heat loads, and surface contamination. Each of these effects can reduce the overall lifespan of the spacecraft. Accurate modeling of plume impingement is an important factor in spacecraft design.

Numerical simulations of thruster plumes can be used to characterize and predict impingement effects. At the extremely low densities seen in a plume expanding into vacuum, continuum fluid mechanics becomes invalid. The direct simulation Monte Carlo (DSMC) method simulates the gas at the microscopic level and can capture nonequilibrium effects occurring

in a rarefied plume flow. DSMC has been successfully applied to nonequilibrium flows in propulsion, hypersonics, and materials processing,¹⁻⁴ as well as to plume impingement flows.^{5,6}

The goal of this work is to validate the capability to simulate complex plume impingement flows using the DSMC technique. To demonstrate this capability, two different three-dimensional impingement flows are examined. The first flow considered is the impingement of a jet on an inclined flat plate. Experimental measurements of impingement quantities are used to verify the numerical results. The second flow is the impingement of a hydrazine thruster plume on a solar array in a model satellite configuration. Free molecular theory is used to model both flows analytically.

Numerical Method

The simulations presented in this study are performed using a three-dimensional version of MONACO, a numerically efficient implementation of the DSMC method.⁷ MONACO is a general-purpose DSMC code designed for workstation architectures. It is designed to be applicable to a wide range of flow problems without requiring problem-specific modifications. It can be run on a single machine or in parallel on an arbitrary number of processors.

Free Molecular Analysis

In the far field of a low-density plume expansion, the flow reaches very low densities and large Knudsen numbers. Under these highly rarefied conditions, the plume can be reasonably approximated as being collisionless. With this assumption, impingement quantities on a surface located within the plume can be calculated analytically. This free molecular analysis provides a limiting case for surface quantities.

Under the assumption of free molecular flow, surface quantities are a function only of the incoming freestream particles. Particles scattering off of the surface do not have any further interaction with the surface or the incoming gas. The net mass, momentum, and energy transferred to the surface is obtained by integrating over the incoming and outgoing particle distribution functions.⁸

If the incoming gas is assumed to have an equilibrium velocity distribution at the hypersonic limit, the pressure is given by

$$p = \frac{1}{2} \rho U^2 \{ 2(2 - \sigma)(\sin \alpha)^2 + \sigma \sqrt{\pi[(\gamma - 1)/\gamma]} \sqrt{(T_w/T_0) \sin \alpha} \} \quad (1)$$

Similar expressions are obtained for shear stress, heat transfer, and flux.

Presented as Paper 98-2755 at the AIAA/ASME 7th Joint Thermophysics and Heat Transfer Conference, Albuquerque, NM, June 15-18, 1998. Copyright © 1999 by the American Institute of Aeronautics and Astronautics, Inc. All rights reserved.

*Graduate Student, Mechanical and Aerospace Engineering Department. Student Member AIAA.

†Associate Professor, Mechanical and Aerospace Engineering Department. Member AIAA.

In the hypersonic limit, the fluid velocity is further approximated by the limiting result from isentropic theory, $U_{\text{lim}} = \sqrt{2C_p T_0}$.

The density of the gas is modeled using the plume model of Simons.⁹ This model describes the density as a function of the throat density and location in the plume expressed in polar coordinates measured from the center of the exit plane. The plume density is given by

$$\rho(r, \theta)/\rho^* = A_p(r^*/r)^2 f(\theta) \quad (2)$$

$$f(\theta) = \{\cos[(\pi/2)(\theta/\theta_{\text{lim}})]\}^{2/(\gamma-1)}, \quad \theta \leq \theta_0 \\ f(\theta = \theta_0)e^{-C(\theta-\theta_0)}, \quad \theta_0 < \theta < \theta_{\text{lim}} \quad (3)$$

where θ_0 is the angle between the plume axis and the streamline separating the boundary layer from the isentropic core, and θ_{lim} is the maximum turning angle of a streamline at the exit for inviscid flow. The constant C is given by

$$C = \frac{3}{2} A_p \sqrt{(\gamma+1)/(\gamma-1)} (R_E/2\delta_E)^{(\gamma-1)/(\gamma+1)} \quad (4)$$

These parameters are calculated analytically as a function of the stagnation conditions, gas properties, and source geometry.¹⁰

The relations for plume density and velocity can be used with expressions for surface quantities such as Eq. (1) to obtain expressions for impingement quantities in terms of distance from the orifice, location in the plume, and the angle of incidence:

$$p = p_0 A_p f(\theta) \left(\frac{r^*}{r} \right)^2 \left(\frac{2}{\gamma+1} \right)^{1/(\gamma-1)} \left(\frac{\gamma}{\gamma-1} \right) \\ \times \left[2(2-\sigma)(\sin \alpha)^2 + \sigma \sqrt{\pi \frac{\gamma-1}{\gamma} \frac{T_w}{T_0}} \sin \alpha \right] \quad (5)$$

$$\tau = 2\sigma p_0 A_p f(\theta) \left(\frac{r^*}{r} \right)^2 \left(\frac{2}{\gamma+1} \right)^{1/(\gamma-1)} \left(\frac{\gamma}{\gamma-1} \right) \cos \alpha \sin \alpha \\ q'' = \sigma \sqrt{2RT_0} p_0 A_p f(\theta) \left(\frac{r^*}{r} \right)^2 \left(\frac{2}{\gamma+1} \right)^{1/(\gamma-1)} \\ \times \sqrt{\frac{\gamma}{\gamma-1}} \left[\frac{\gamma}{\gamma-1} - \frac{\gamma+1}{2(\gamma-1)} \frac{T_w}{T_0} \right] \sin \alpha \quad (6)$$

$$F = nU \\ = \frac{p_0}{m} A_p f(\theta) \left(\frac{r^*}{r} \right)^2 \left(\frac{2}{\gamma+1} \right)^{1/(\gamma-1)} \sqrt{\frac{2}{RT_0} \frac{\gamma}{\gamma-1}} \quad (7)$$

Inclined Flat Plate

Impingement of a jet onto an inclined flat plate represents one of the simplest possible three-dimensional impingement problems. The relatively simple geometry allows it to be readily investigated both numerically and experimentally while still retaining three-dimensional effects.

The problem under consideration is a freejet impacting on a flat plate. A plume of molecular nitrogen is generated by a sonic orifice. The orientation of the plate is varied relative to the axis of the plume. Figure 1 shows a schematic of the configuration.

This study considers one particular set of orifice inlet conditions—unheated flow ($T_0 = T_w = 300$ K) expanding from a stagnation pressure of 1000 Pa. The orifice itself is circular in cross section and 1 mm in radius, and the flow is assumed to be sonic at the exit. The Knudsen number based on orifice radius is 8×10^{-3} at the orifice exit. These conditions ensure a rarefied plume flow suitable for calculation using the DSMC

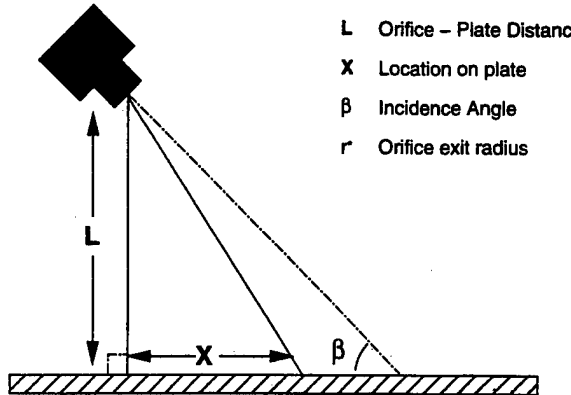


Fig. 1 Schematic of flat-plate impingement.

method. The impingement surface is located a distance of 40 mm from the orifice measured perpendicular to the surface (distance L in Fig. 1). The flow conditions and geometry yield a plume constant $A_p = 0.617$ and a turning angle $\theta_{\text{lim}} = 130.5$ deg.

Experimental Study

The plate impingement configuration was investigated experimentally at DLR, German Aerospace Research Center, Germany. Measurements of impingement pressure and shear stress were taken by Legge,¹¹ and measurements of heat flux were made by Döring.¹² A variety of stagnation pressures, plate orientations, and separations were considered.

Pressure and shear stress data were obtained using a pressure balance that directly measured the force on a floating element. Heat flux data were obtained by measuring the rate of change of surface temperature using thermocouples. Data were taken on the surface along a line that is coplanar with the plume axis.

The experiments were performed in the high vacuum facility in Göttingen, Germany. The background pressure of the facility was 0.045 Pa during pressure and shear measurements with the stagnation pressure considered in the present study (1000 Pa). The background pressure was twice this value (0.090 Pa) during the heat transfer experiment.

Pressure and shear-stress data were normalized to eliminate the effect of stagnation pressure and plate separation L . The following normalizations were used:

$$\hat{p} = (p/p_0)(L/r^*)^2 \quad (8)$$

$$\hat{\tau} = (\tau/p_0)(L/r^*)^2 \quad (9)$$

While this normalization does reduce the data to a significant degree, some dependence on the stagnation pressure is still observed. A reduction in stagnation pressure results in an increase in normalized pressure and shear stress as a result of the increasing rarefaction of the plume. For the present study, data obtained using a stagnation pressure of 1000 Pa are used whenever possible.

Physical Modeling

The inlet flow at the sonic orifice is modeled as a macroscopically uniform stream of molecular nitrogen directed along the axis of the plume. The effects of a boundary layer at the exit are assumed to be small and are neglected. Inlet properties are calculated from isentropic theory assuming sonic conditions at the exit and stagnation conditions of 1000 Pa and 300 K. This corresponds to a velocity of 323 m/s, a temperature of 252.2 K, and a number density of $1.53 \times 10^{23} \text{ m}^{-3}$. A background gas pressure is imposed to simulate the effects of the experimental tank pressure.

The impingement surface is modeled assuming diffuse reflection with full accommodation to a constant surface tem-

perature ($\sigma = 1.0$). The surface temperature is equal to the stagnation temperature of the plume (300 K).

Computational Modeling

Fully unstructured grids using tetrahedral cells are used. Grids are generated using an advancing front package called FELISA. Cell sizes are approximately scaled to the local mean free path. Figure 2 shows an example of a grid for the case with the plume axis parallel to the surface ($\beta = 0$ deg). Only the boundary mesh is shown. The majority of cells are in the vicinity of the nozzle where the density is highest. Compression at the surface is relatively small because of the low densities involved. As a result, the surface grid at the plate (not shown) consists of approximately uniform triangles for the cases considered. Symmetry planes are employed to reduce the size of the domain. Two planes are used in the normal impingement ($\beta = 90$ deg) case, and one each in the other cases.

The simulation time step is varied across the domain, with each cell using a unique value. The local time step is scaled by the cell size that is approximately proportional to the inverse of the local density.

Simulations are load balanced for parallel execution using a simple scheme that groups cells according to the Z coordinate of their geometric center. The number of cells assigned to each processor is chosen to distribute particles evenly among processors.

Typical parameters for the three-dimensional plume simulations are summarized next. Computational cost parameters for plate impingement: grid cells = 300,000; number of particles = 3.5 million; transient steps = 22,500; sampling steps = 5,000; calculation time = 14 h; and steady state $\eta_s = 95\%$. The calculations are performed using 16 nodes of an IBM SP-2.

Comparison of Surface Quantities

Impingement quantities are examined for several orientations of the plate. Comparison with experimental data is used to verify the accuracy of the DSMC simulations of the plume and impingement. Comparison with predictions from the free molecular model provides an estimate of the accuracy of this theory for simple impingement flows as well as a qualitative basis for comparison with the simulation at the far ends of the surface where experimental data are not available.

In the case of normal impingement of the plume ($\beta = 90$ deg), the experimental data are taken along a radial line extending out from the axis. The simulation data set includes data across the entire surface presented as a function of distance from the axis. In the other cases, both the experimental and simulation data sets are taken along a line on the surface that is coplanar with the plume axis.

Normal Impingement ($\beta = 90$ Deg)

Figure 3 compares normalized surface pressures for simulation, experiment, and free molecular theory. Good agreement is found between the data sets. The profiles show the same

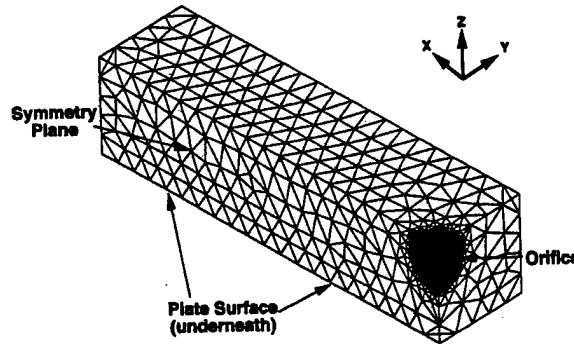


Fig. 2 Surface grid for $\beta = 0$ -deg case.

general shape: pressure falling from a maximum at the axis. The DSMC and theoretical profiles show an asymptote at the background pressure at large distances from the axis, where the plume has a minimal effect on the surface.

The simulation underpredicts the experimental values by a significant amount (as much as 60%) at the far extent of the experimental data set. The smooth asymptotic shape seen in the DSMC and theoretical profiles is not as apparent in the measurements far from the axis. The slower decrease in pressure with distance from the axis may indicate difficulties in measuring pressures at the low densities away from the axis. It may also indicate a higher tank pressure in the facility than is reported.

Normalized shear stress is considered in Fig. 4. Good agreement is observed between the simulation, experiment, and theory. The profiles each show the same shape with stress rising from zero at the plume axis to a maximum and then falling with decreasing gas pressure. DSMC stresses exceed the free molecular values far from the axis. This is likely a result of particles that strike the surface, undergo collisions with the incoming plume, and are scattered back to the surface at a high angle of attack.

Surface heat flux is shown in Fig. 5. The simulation captures the trend of the experimental measurements and predicts the magnitude of the heat flux away from the axis. The simulation does overpredict the heat flux considerably near the axis ($X/L < 0.75$).

Significant fluctuations appear in the numerical heat-flux results, with the magnitude of the fluctuations increasing with distance from the axis. This is primarily a result of the sample size of particles striking the surface. The total number of particles sampled per cell is on the order of 10^4 near the axis and

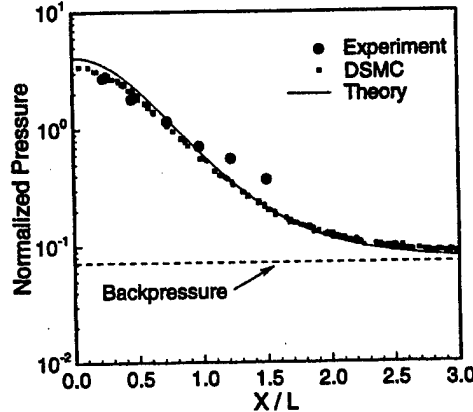


Fig. 3 Comparison between DSMC and measured surface pressures at $\beta = 90$ deg.

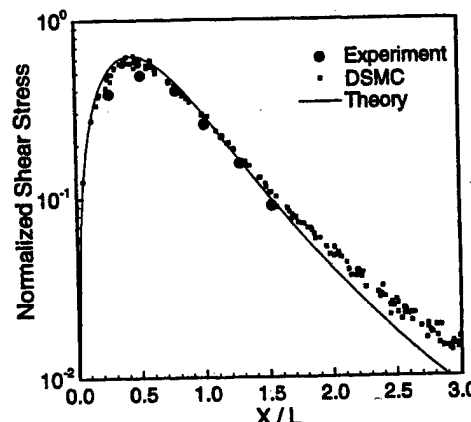


Fig. 4 Surface shear stress for $\beta = 90$ deg. Comparison between DSMC, experiment, and free molecular theory.

decreases with radial distance, up to a factor of 3 at the farthest radial extent. The statistical fluctuations in the DSMC simulation are magnified in the calculation of energy transfer that involves the second moment of the particle velocities.

The theoretical curve has the same shape as the DSMC result, but shows a larger magnitude of heat transfer. The difference increases as the axis is approached. Gas densities are larger near the axis, and consequently, the mean free path and Knudsen number are smaller. The assumption of free molecular flow is weakest near the axis and collisional effects are more significant. This tends to lower the energy transfer below the free molecular value. The deviation is greater in terms of heat transfer than in pressure or shear stress because energy is a second moment of the particle distribution function.

$\beta = 45$ -Deg Case

Figure 6 shows surface pressure profiles for the $\beta = 45$ -deg case. Good agreement is again found between the simulation and experimental data sets as well as free molecular theory. The point of maximum pressure is just downstream of the point directly below the orifice, where the effects of density and angle of attack are high. The pressure drops off asymptotically to the background value to both sides of this maximum; this is more rapid behind the orifice.

The experimental data are again higher than the DSMC and theoretical values at both ends of the profile. The magnitude of the pressures at these points are comparable to that seen at the end of the $\beta = 90$ -deg profile. This points toward uncertainty in pressure measurements at low densities or a higher back pressure in the facility.

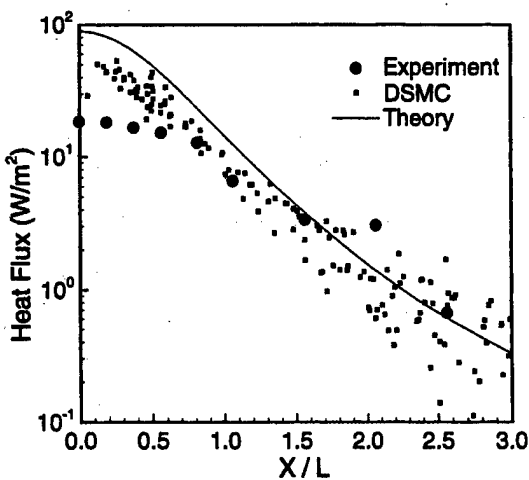


Fig. 5 Surface heat flux for $\beta = 90$ deg. Comparison between DSMC, experiment, and free molecular theory.

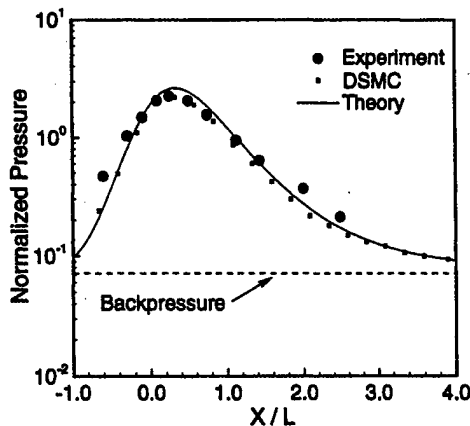


Fig. 6 Surface pressure for $\beta = 45$ deg. Comparison between DSMC, experiment, and free molecular theory.

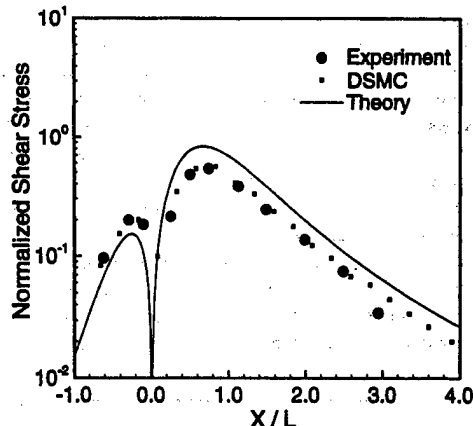


Fig. 7 Surface shear stress for $\beta = 45$ deg. Comparison between DSMC, experiment, and free molecular theory.

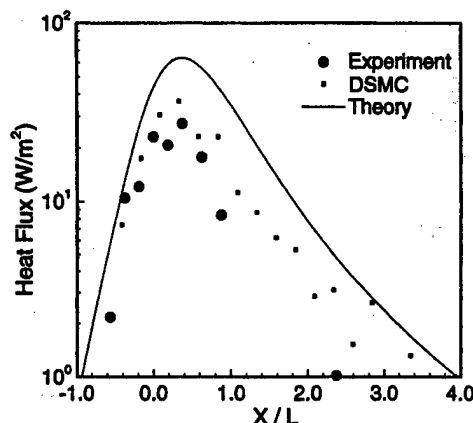


Fig. 8 Surface heat flux for $\beta = 45$ deg. Comparison between DSMC, experiment, and free molecular theory.

Shear-stress profiles are reported in Fig. 7. The DSMC stresses show excellent agreement with the experimental data. The features of the experimental profile are captured by the simulation, particularly the rapid decrease that occurs directly below the orifice.

While the qualitative structure of the free molecular profile agrees with those of the simulation and experiment, the theoretical profile differs in terms of magnitude. In front of the orifice ($X/L > 0$), the free molecular stresses overpredict the simulation and measured values. Behind the orifice ($X/L < 0$), the free molecular stresses underpredict the actual stresses. This is likely a result of the presence of backscattered particles that strike the surface behind the orifice.

Heat transfer profiles are reported in Fig. 8. Although significant fluctuations are again seen in the simulation and experimental results, there is generally good agreement between the data sets. Free molecular theory overpredicts heat transfer across most of the range considered because of collisional effects. This effect is countered to some extent behind the orifice by backscattered particles that tend to increase the transport of energy to the surface.

Parallel Impingement ($\beta = 0$ Deg)

Before presenting comparisons with experimental data, it is important to note that the DLR study by Legge¹¹ does not report pressure or shear-stress data for the parallel impingement case with a stagnation pressure of 1000 Pa. The lowest stagnation pressure for which $\beta = 0$ -deg pressure and shear data are reported is 4000 Pa. The study by Döring¹² does present heat flux data for a stagnation pressure of 1000 Pa. The DSMC simulations use a stagnation pressure of 1000 Pa. Although the data are normalized by the stagnation pressure,

Legge reports some effect of flow rarefaction on the normalized surface quantities, particularly shear stress.

The difference in stagnation pressures complicates the modeling of tank pressure effects. The ratio of background to stagnation pressure is not a constant in the experimental facility, generally falling with increasing stagnation pressure. Consequently, the parallel impingement case has been simulated without backpressure and the theoretical pressure profile is for expansion into a vacuum.

Surface pressures for the parallel impingement case are shown in Fig. 9. The profiles show good qualitative agreement. Without a backpressure, the simulation and theoretical profiles drop toward zero at the ends of the plate. No asymptote is seen

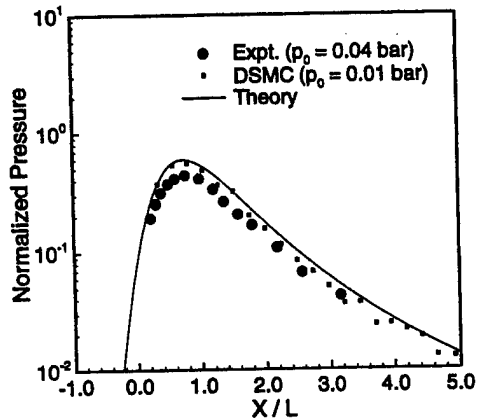


Fig. 9 Surface pressure for $\beta = 0$ deg. Comparison between DSMC, experiment, and free molecular theory.

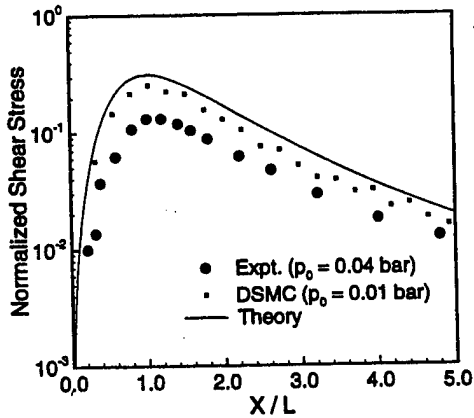


Fig. 10 Surface shear stress for $\beta = 0$ deg. Comparison between DSMC, experiment, and free molecular theory.

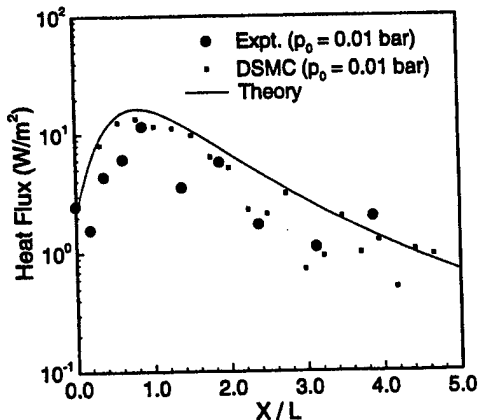


Fig. 11 Surface heat flux for $\beta = 0$ deg. Comparison between DSMC, experiment, and free molecular theory.

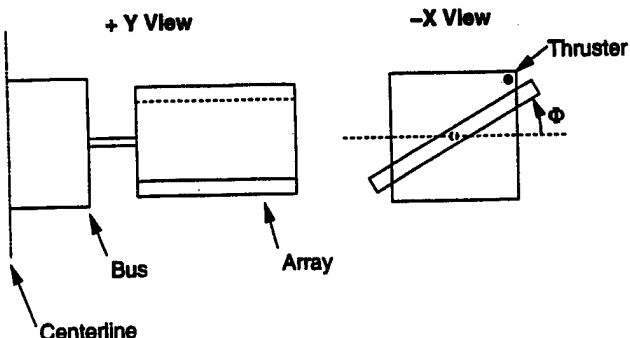


Fig. 12 Schematic of model satellite configuration.

in the experimental data because the normalized facility pressure (not shown) is significantly lower with the higher stagnation pressure. The lower experimental pressures are a result of a higher stagnation pressure and lower Knudsen number at the surface.

Shear stress data are shown in Fig. 10. The profiles again show qualitative agreement. The experimental values are lower because of higher densities. The effect on shear is stronger than that on pressure. This was previously reported by Legge.¹¹ The effect of rarefaction can be seen to a much smaller degree in a comparison between simulation and free molecular results. The DSMC values are slightly lower because of collisional effects.

Heat transfer results are presented in Fig. 11. Experimental heat-flux data are based on a stagnation pressure of 1000 Pa, equal to that used in the DSMC simulation. At the low densities involved in the parallel impingement case, statistical fluctuations are quite large in both the experimental and numerical results. The simulation results overpredict the data to some degree, although the trend is captured quite well. The free molecular results do not significantly overpredict the heat transfer as was seen in the other cases. This is likely a result of the low densities found at the surface for this case.

Model Satellite Configuration

A representative satellite geometry consisting of a spacecraft bus and solar arrays is simulated as a model impingement configuration. A plume is generated by a hydrazine control thruster mounted at the corner of one side of the spacecraft bus. Fig. 12 shows a schematic of the problem. The spacecraft bus is a 1.5-m cube of which half is simulated. The array section is 3.25 m long, 2.5 m wide, and 0.12 m thick, and is deployed 0.75 m from the spacecraft. Expansion of the plume and its impingement on the solar array panel are modeled. Two orientations of the array with respect to the bus are considered.

The thruster is modeled after an operating hydrazine control thruster, the MR-103-series 0.2-lbf REA, manufactured by Primex Aerospace Company. This thruster was originally developed for the Voyager 1 and 2 spacecraft and is also in use on such programs as GPS, Iridium, Cassini, and various communications satellites. This study will consider an operating mode at 60% of the rated thrust. Relevant data for the thruster^f are shown next: Operating conditions and parameters for hydrazine thruster: nominal thrust = 0.55 N, expansion ratio = 100:1, half angle = 15 deg, exit radius = 2.921 mm, chamber pressure = 1.25 MPa, stagnation temperature = 1167 K, and flow rate = 2.62×10^{-4} kg/s.

Physical Modeling

The gas plume is a three-species mixture of molecular nitrogen, hydrogen, and ammonia. Simulations begin at the exit plane of the thruster using flow properties based on a numerical calculation of flow in the thruster. Exit plane number densities

^fMorris, J., private communication, Primex Aerospace Co., Redman, WA, 1997.

taken from this earlier calculation are scaled down by a factor of 1.52 to maintain consistency with the experimentally measured mass flow of the device. At the centerline the inlet flow has the following properties: 2200 m/s velocity, 500 K temperature, and $3.2 \times 10^{23} \text{ m}^{-3}$ total density.

Because of the relatively low temperature of the plume, it can be considered chemically frozen. Vibrational energy modes are likewise frozen. All spacecraft surfaces are modeled as diffuse reflectors with full accommodation. Surfaces are maintained at 273 K. Surface chemistry and adsorption are not considered in these calculations.

Computational Modeling

Simulations are performed in two parts. First, an axisymmetric calculation of the near-field plume in the vicinity of the thruster is performed. Data from this calculation are then used as input for the three-dimensional calculation of the plume far field and impingement. Separation of the calculation in this manner greatly reduces the cost of the overall calculation.

Near Field

The near field expansion of the plume is considered to be an axisymmetric problem that is independent of the surrounding geometry. The flow domain is hemispherical and extends more than 10 exit radii out from the center of the thruster exit. The grid is an unstructured mesh with cell sizes and time steps scaled according to the local mean free path.

Inflow conditions for the far-field calculation are taken at the breakdown surface. This is the locus of points for which the breakdown parameter¹³ equals the threshold value $P = 0.02$. To more readily use this as a geometric interface between the near- and far-field simulations, the surface is simplified to a capped cylinder with uniform cross section. Density in the near

field is shown in Fig. 13 along with the location of the interface surface.

Far Field and Impingement

The far-field simulation considers the whole area surrounding the spacecraft, including the solar array. The computational domain is an orthogonal parallelepiped that extends beyond the spacecraft surface by at least 0.25 m in each coordinate direction. Only one-half of the spacecraft is simulated. The boundaries of the computational domain are shown in Fig. 14. The solar array is shown in the nominal, unrotated configuration ($\Phi = 0$ deg).

An unstructured mesh consisting of tetrahedral cells is employed. The mesh is generated using the grid-generation package FELISA. Cell sizes are approximately scaled according to local density. Variable time steps are employed with cell size being used as a scaling factor.

To improve resolution in the vicinity of the interface surface where flow density is highest, a simple scheme of particle weight scaling is employed. Cells in the immediate vicinity of the inflow (interface) surface are assigned a low particle weight, 10% of the reference value for the simulation. The band of cells immediately outside this surface are assigned a weight of 40% of the reference value. The remaining cells are assigned the reference weight. Figure 15 shows this weight scheme on a plane cut taken along the axis of the cylindrical inflow surface. This scaling roughly follows the density variation in close proximity to the inflow. Because there is only a small number of particles moving toward the inflow in this highly supersonic flow, there is a minimal amount of cloning involved. The weight scheme allows reasonable resolution of the high-density region without affecting the accuracy of the calculation.

The computational parameters for the near- and far-field plume calculations are summarized in Table 1.

Results

Impingement simulations were performed for two orientations of the solar array, $\Phi = 0$ deg and $\Phi = +30$ deg. Of

Table 1 Computational cost parameters for model satellite configuration

Parameter	Near field	Far field
Grid size	7600 cells	290,000 cells
Number of particles	425,000	2,900,000
Transient steps	12,500	18,000
Sampling steps	10,000	10,000
Calculation time	5 h	11 h
Number of processors	4	16
Parallel efficiency	97%	91%

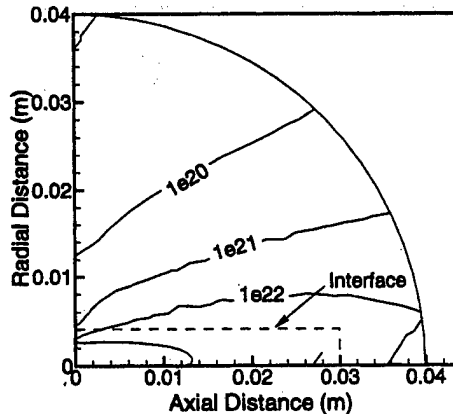


Fig. 13 Contours of number density for the axisymmetric near-field simulation. The interface surface is indicated.

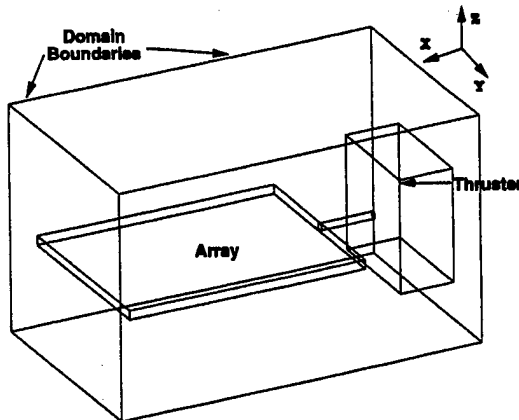


Fig. 14 Boundaries of the computational domain. Shown for unrotated array case, $\Phi = 0$ deg.

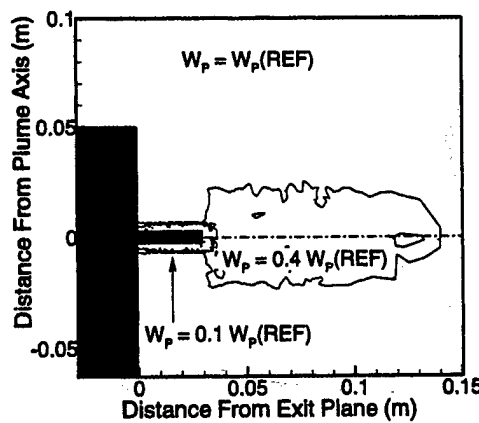


Fig. 15 Particle weight scaling in the vicinity of the inflow surface.

primary importance are the mass, momentum, and energy imparted to the array by the plume. Figures 16 and 17 show distributions of surface pressure for the 0- and +30-deg cases. The view is in the plane of the array. The contour plots show maximum values at the near end of the array toward the +Y side, closest to the thruster. In the $\Phi = 0$ -deg case, the maximum pressure is downstream of the leading edge as a result of the influence of the nozzle boundary layer. As expected, impingement pressures are larger in the $\Phi = +30$ -deg case, where the array is tilted toward the thruster.

Ammonia molecules are the major contamination concern with hydrazine thrusters. Figures 18 and 19 show distributions of ammonia flux on the array. The qualitative behavior of this property is very similar to that observed with pressure.

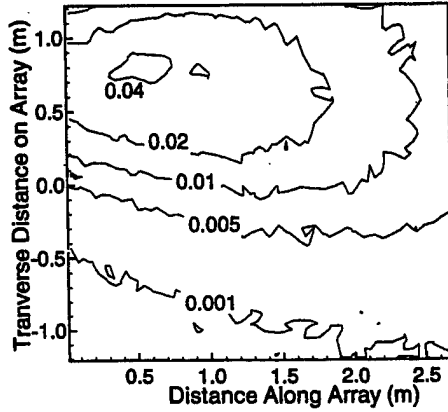


Fig. 16 Contours of impingement pressure (Pa) at the array surface for the 0-deg array case.

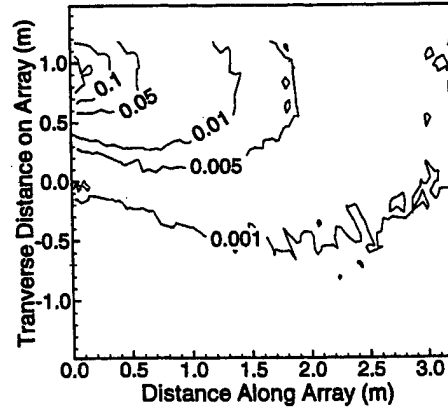


Fig. 17 Contours of impingement pressure (Pa) at the array surface for the 30-deg array case.

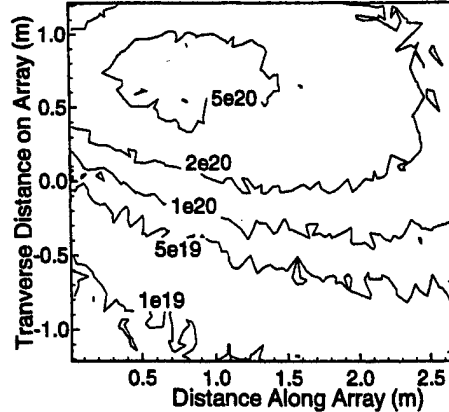


Fig. 18 Contours of NH_3 flux ($\text{no./m}^2 \text{ s}$) at the array surface for the 0-deg array case.

Data extracted along a line on the array surface are used to quantitatively examine the surface quantities. Data are taken on the line that intersects the array top surface and the plane parallel to the array axis that contains the plume axis.

The operating conditions for the hydrazine thruster can be used to calculate the plume parameters A_P , θ_{lim} , θ_0 , and C . There is some uncertainty involved in this calculation when a multispecies gas is considered. To be most useful from an engineering standpoint, the free molecular results should be based on stagnation conditions and the geometry of the nozzle. The expressions for surface quantities [Eqs. (5–7)] depend on gas properties R and γ , which are difficult to determine a priori for a rarefied gas in which individual species will have varying mole fractions and velocities. In this study, the gas has been

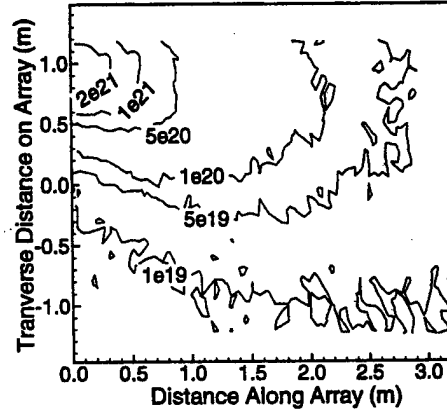


Fig. 19 Contours of NH_3 flux ($\text{no./m}^2 \text{ s}$) at the array surface for the 30-deg array case.

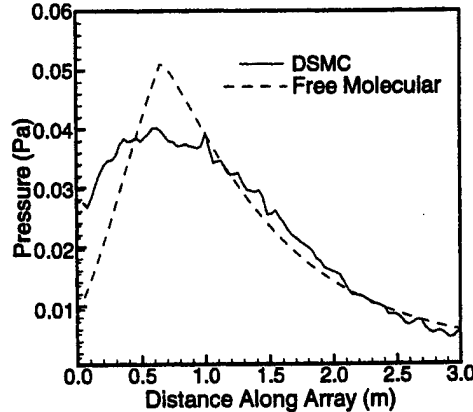


Fig. 20 Comparison of simulation and free molecular pressures on array surface for 0-deg array case.

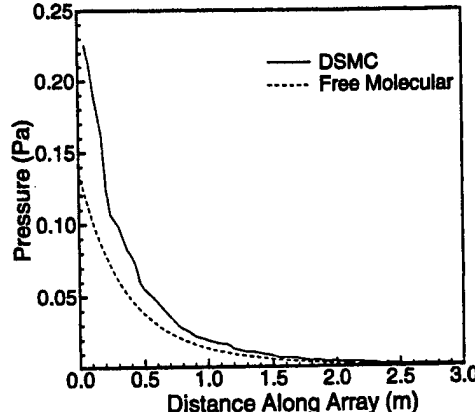


Fig. 21 Comparison of simulation and free molecular pressures on array surface for 30-deg array case.

assumed to have a constant molecular weight and ratio of specific heats using values reported for the exit plane ($M = 13$ kg/mol, $\gamma = 1.4$). These parameters yield a plume constant, $A_p = 3.62$, boundary-layer constant, $C = 12.6$, and limiting angle, $\theta_0 = 19.2$ deg and $\theta_{lim} = 58.7$ deg.

Figure 20 shows impingement pressure profiles for the 0-deg case. Reasonable agreement is found on the far end of the array, but at the near end the free molecular result falls well below the simulation. The noticeable drop in the free molecular profile on the upstream side of the array is a result of boundary-layer effects. The drop in pressure can be seen in the simulation as well, but it is not as dramatic. The sharp decline indicates that the density model falls too rapidly in the boundary-layer regime.

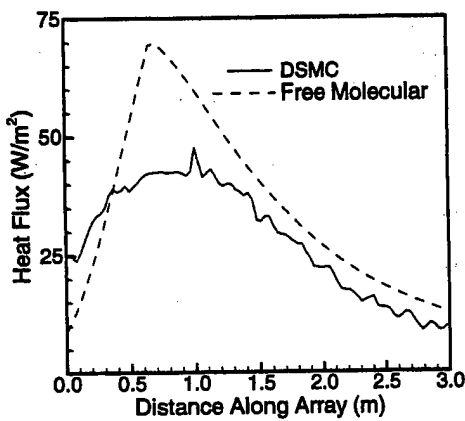


Fig. 22 Comparison of simulation and free molecular heat flux on array surface for 0-deg array case.

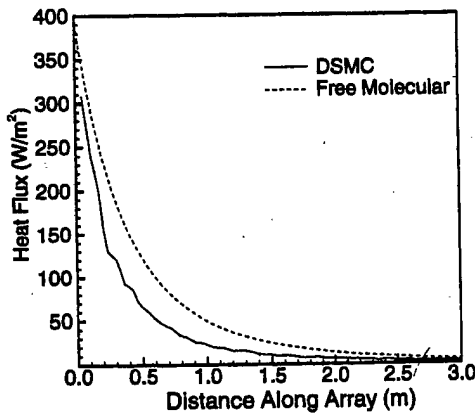


Fig. 23 Comparison of simulation and free molecular heat flux on array surface for 30-deg array case.

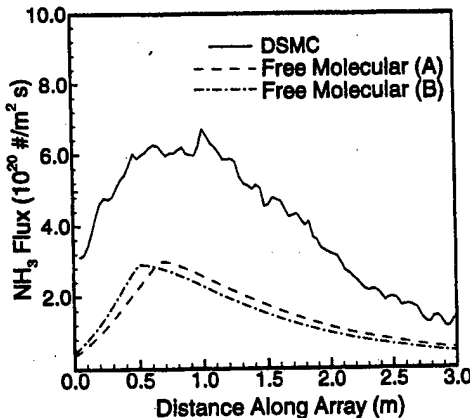


Fig. 24 Comparison of simulation and free molecular NH₃ flux on array surface for 0-deg array case.

The 30-deg case is shown in Fig. 21. In this case, the array is rotated toward the thruster, and as a result the profile being considered is significantly closer to the thruster. The linear profile is within the core of the plume, and consequently, there is no drop in pressure on the upstream side of the plate as a result of the boundary layer. Both the simulation and analytical profiles primarily show an inverse squared drop in pressure with distance, which is consistent with the density model. The DSMC results predict a 70% higher pressure across the length of the array. This may indicate a low estimate of the plume constant A_p .

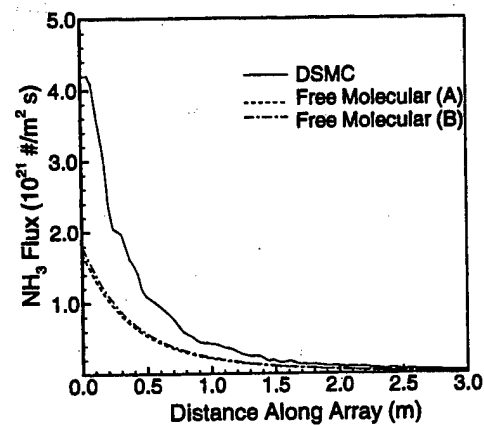


Fig. 25 Comparison of simulation and free molecular NH₃ flux on array surface for 30-deg array case.

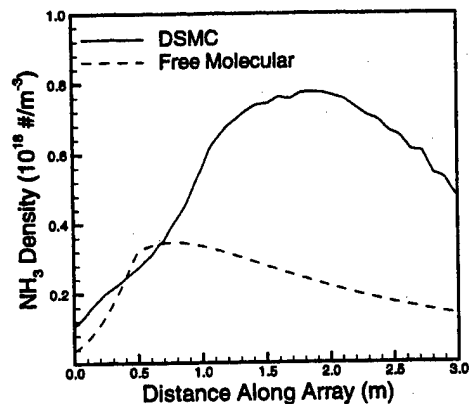


Fig. 26 Comparison of NH₃ densities from stand-alone plume simulation and free molecular model. Data at location of array surface for 0-deg case.

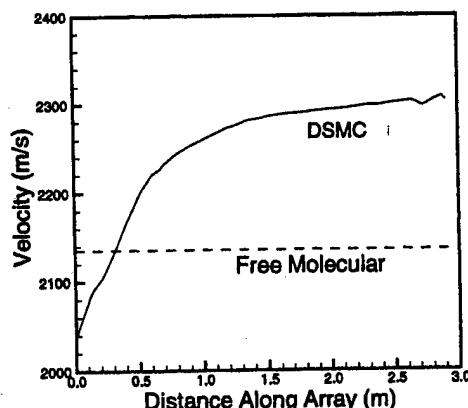


Fig. 27 Comparison of NH₃ velocities from stand-alone plume simulation and free molecular model. Data at location of array surface for 0-deg case.

Figures 22 and 23 show heat transfer profiles. In both cases the behavior is very similar to that of surface pressure. The free molecular profile for 0 deg shows an extreme drop on the upstream end while otherwise matching the shape of the DSMC profile. In the 30-deg case the DSMC and theoretical profiles are qualitatively similar. In both cases the free molecular values tend to exceed the simulation heat transfer. Overprediction of heat flux is consistent with the results for flat-plate impingement.

The number density flux of ammonia striking the array is shown in Figs. 24 and 25. Two free molecular profiles are shown for each case. The first (labeled A) assumes a constant species composition in the plume model and a uniform limiting velocity based on the average molecular weight. The second (B) calculates the ammonia flux as if the plume was composed entirely of ammonia with the correct number density. The two methods produce essentially the same fluxes.

Qualitatively, the flux profiles show the same behavior for both pressure and heat transfer. Both angle cases show significantly higher DSMC fluxes. This indicates the difficulty of applying the free molecular model to a multispecies, rarefied gas.

The problems with the free molecular model for flux are illustrated by a simulation of the thruster plume flowfield without any impingement surfaces. This plume flow should give a reasonable estimate of what the impingement surfaces see, because the boundary layer caused by the impingement is small. Figure 26 plots ammonia density for the freely expanding plume at the same spatial location as the linear profiles shown for the 0-deg case in Fig. 24. The DSMC results are compared with density predicted by the Simons plume model (assuming an ammonia plume, method B discussed earlier).

Figure 27 compares simulated ammonia velocities and the limiting velocity employed in the free molecular analysis ($\sqrt{2C_p T_0}$). Downstream of where the leading edge of the solar array would be located, within the isentropic core of the plume, DSMC densities are on average two times higher than the Simons model predicts. DSMC velocities are also 5–8% larger

than the analytical model. Because the number density flux in free molecular flow is the product of density and velocity [Eq. (7)], these factors combine to produce the significantly larger fluxes seen in the DSMC results shown in Fig. 24.

In the boundary-layer region, the relationship between plume properties and impingement flux is less clear. However, near the upstream edge, the simulation again produces significantly higher ammonia densities, which again would lead to larger flux. The more complex density profile seen in the DSMC result, likely caused by differing mole fractions and velocity slip between the species, again indicates the limitations of the analytical plume model for complex gas flows.

The total forces and torques imparted to the array are important for spacecraft design. The total amount of a contaminant such as ammonia striking the surface is also important. Tables 2 and 3 summarize these integrated quantities for the two simulations. Integrated quantities calculated from free molecular theory are also included.

It is worthy to note that in both cases the net force exerted on the array by the plume is on the order of 20% of the nominal 0.55 N thrust of the thruster. This interaction force is primarily in the +X direction, which is opposite to the thrust vector and thus acts to reduce the effective thrust of the device. As a result, nearly 20% of the propulsion energy is wasted.

Little net difference is seen between the two array orientations. Although part of the array is closer to the thruster in the 30-deg case, the average angle of attack over the array is higher, which reduces the impingement quantities. The rotation causes a portion of the array to be significantly farther from the thruster, reducing the effective area over which force is exerted.

Comparison between the simulation and free molecular values follows the same pattern shown in the linear profiles. The net forces are comparable, which is consistent with similar pressures. Free molecular flow predicts a higher energy transfer and a significantly lower net flux of ammonia, both consistent with the previous comparisons.

In all of the previous analyses and simulations, surfaces were assumed to be fully accommodating. A more accurate representation of a real surface would assume partial accommodation. An accommodation coefficient σ of 0.8 is typical for a metallic surface. Table 4 compares integrated impingement effects for full and partial accommodation. As expected, net heat transfer to the array scales with accommodation coefficient. The net force in the x direction, parallel to the plume axis, is a result of surface shear, and consequently, also scales with σ . The other two force components and torque are essentially unaffected by a change in accommodation coefficient. These quantities are primarily caused by surface pressure that scales nonlinearly with σ .

Examination of the comparisons in Table 4 and the expression for impingement pressure [Eq. (5)] indicate that the surface model will have some effect on the net impingement effects. Heat transfer will be overpredicted by a fully diffuse model. Momentum transfer will be overpredicted if it is primarily a result of shear forces. If more direct impingement is involved, such as might occur in a docking maneuver, the effect is less clear and will depend on the surface and plume temperatures and the geometry through angle of attack. These

Table 2 Integrated impingement effects for $\Phi = 0$ deg

Impingement property	DSMC	Free molecular
Net force, X component, N	0.100	0.118
Net force, Y component, N	-0.0107	-0.00588
Net force, Z component, N	-0.0814	-0.0647
Net centerline torque, Nm	0.0405	0.0369
Net heat transfer, W	101	112
Net incidence of NH_3 , s^{-1}	1.44×10^{21}	470×10^{20}

Table 3 Integrated impingement effects for $\Phi = +30$ deg

Impingement property	DSMC	Free molecular
Net force, X component, N	0.0922	0.148
Net force, Y component, N	0.0228	0.0226
Net force, Z component, N	-0.0645	-0.0563
Net centerline torque, Nm	0.0519	0.0509
Net heat transfer, W	88.3	137
Net incidence of NH_3 , s^{-1}	1.43×10^{21}	6.15×10^{20}

Table 4 Effect of accommodation coefficient on free molecular integrated impingement effects

Impingement property	$\Phi = 0$ deg, $\sigma = 1.0$	$\Phi = 0$ deg, $\sigma = 0.8$	$\Phi = +30$ deg, $\sigma = 1.0$	$\Phi = +30$ deg, $\sigma = 0.8$
Net force, X component, N	0.118	0.0945	0.148	0.118
Net force, Y component, N	-0.00588	-0.00471	0.0226	0.0227
Net force, Z component, N	-0.0647	-0.0656	-0.0563	-0.0531
Net centerline torque, Nm	0.0369	0.0377	0.0509	0.0490
Net heat transfer, W	112	89.5	137	109

observations should hold for both an analytical model and DSMC simulations.

Conclusions

The DSMC method provides reasonably accurate modeling of impingement flows. Generally good agreement with experimental data for the plate problem indicates that the plume and impingement effects are modeled correctly, although there is some tendency to overpredict surface heat flux. The calculation of a satellite configuration demonstrates the ability to simulate real engineering configurations. Calculations are expensive in three dimensions, but can be performed efficiently in parallel. Careful use of variable scaling can reduce the overall cost significantly.

Free molecular theory provides a reasonable estimate of surface quantities at high Knudsen numbers. The analysis tends to overpredict the values, however, with heat transfer and shear stress being more sensitive to the degree of rarefaction than pressure. Boundary-layer and multispecies effects are not properly handled by the simple plume model.

Problems that can be broken down into two distinct parts such as the near and far field of a plume can be more efficiently computed using two separate simulations. If the first portion can be computed assuming axial symmetry, the overall cost can be reduced significantly. This type of hybrid approach is particularly appropriate for engineering problems, where simulations of a number of far-field problems may be begun using a single near-field result.

Acknowledgments

The authors gratefully acknowledge the financial support of John H. Glenn Research Center at Lewis Field through Grant NAG3-1451 and the U.S. Air Force Office of Scientific Research under Grant F49620-96-1-0210. Computational resources were provided by the Cornell Theory Center and the National Aerodynamic Simulation program at NASA Ames Research Center.

References

- ¹Boyd, I. D., and Stark, J. P. W., "Modeling of a Small Hydrazine Thruster Plume in the Transition Flow Regime," *Journal of Propulsion and Power*, Vol. 6, No. 2, 1990, pp. 121-126.
- ²Boyd, I. D., Penko, P. F., Meissner, D. L., and DeWitt, K. J., "Experimental and Numerical Investigations of Low-Density Nozzle and Plume Flows of Nitrogen," *AIAA Journal*, Vol. 30, No. 10, 1992, pp. 2453-2461.
- ³Boyd, I. D., Candler, G. V., and Levin, D. A., "Dissociation Modeling in Low Density Flows of Air," *Physics of Fluids*, Vol. 7, No. 7, 1995, pp. 1757-1763.
- ⁴Font, G. J., and Boyd, I. D., "Numerical Study of the Effects of Reactor Geometry on a Chlorine Helicon Etch Reactor," *Journal of Vacuum Science and Technology A*, Vol. 15, No. 2, 1997, pp. 313-319.
- ⁵Ivanov, M. S., Markelov, G. N., Kashkovsky, A. V., and Giordano, D., "Numerical Analysis of Thruster Plume Interaction Problems," *Proceedings of the 2nd European Spacecraft Propulsion Conference*, European Space Agency, SP-398, 1997, pp. 603-610.
- ⁶Lumpkin, F. E., Stuart, P. C., and Le Beau, G. J., "Enhanced Analyses of Plume Impingement During Shuttle-Mix Docking Using a Combined CRD and DSMC Methodology," *AIAA Paper 96-1877*, June 1996.
- ⁷Dietrich, S., and Boyd, I. D., "Scalar and Parallel Optimized Implementation of the Direct Simulation Monte Carlo Method," *Journal of Computational Physics*, Vol. 126, 1996, pp. 328-342.
- ⁸Schaaf, S. A., and Chambré, P. L., *Flow of Rarefied Gases*, Princeton Univ. Press, Princeton, NJ, 1961.
- ⁹Simons, G. A., "Effect of Nozzle Boundary Layers on Rocket Exhaust Plumes," *AIAA Journal*, Vol. 10, No. 11, 1972, pp. 1534, 1535.
- ¹⁰Legge, H., and Boettcher, R. D., "Modelling Control Thruster Plume Flow and Impingement," *Rarefied Gas Dynamics*, Plenum, New York, 1985, pp. 983-992.
- ¹¹Legge, H., "Plume Impingement Forces on Inclined Flat Plates," *Rarefied Gas Dynamics*, VCH Press, Weinheim, Germany, 1991, pp. 955-962.
- ¹²Döring, S., "Experimental Plume Impingement Heat Transfer on Inclined Flat Plates," DLR, German Aerospace Research Center, TR IB 222-90 A 36, Germany, Sept. 1990.
- ¹³Bird, G. A., *Molecular Gas Dynamics*, Clarendon, Oxford, England, UK, 1994.

Particle Simulations of a Hall Thruster Plume

Douglas B. VanGilder,* Iain D. Boyd,[†] and Michael Keidar[‡]
Cornell University, Ithaca, New York 14853

A numerical code that combines the direct simulation Monte Carlo method with the particle-in-cell method has been developed to examine the plumes of Hall thrusters. The present investigation includes a study of the sensitivity of the computed plume to various ion conditions at the thruster exit and considers models for computing the electric field based on the electron momentum equation. Specifically, two electrostatic models are compared: one assumes isothermal electrons, whereas the other uses a variable electron temperature model. Computations are compared with experimental measurements of current density, ion velocity, ion density, electron density, heat flux, and plasma potential in the plume of a stationary plasma thruster. The varying electron temperature is found to affect the very near field significantly. Simulations using this model agree better with near-field current density measurements. This model also leads to better agreement with electron number density measurements in the far field. The agreement of plasma potential depends on parameters used in the simulations. To better represent the flow inside the experimental facilities, the full chamber geometry is simulated assuming symmetry about the thruster centerline. These simulations lead to excellent agreement with current density measurements to 180 deg. The sensitivity study indicates that the far-field current density is relatively easy to reproduce.

Nomenclature

E	= electric field, V/m
e	= charge of an electron, C
k	= Boltzmann constant, J/K
n_j	= number density of species j , m ⁻³
n_{ref}	= reference electron number density, m ⁻³ ; defined where potential is 0
p	= pressure, N/m ²
T_e	= electron temperature, K unless specified as eV
W_j	= particle weight of species j
Xe	= xenon
γ	= ratio of specific heats
ϕ	= plasma potential, V

Subscripts

e	= electrons
f	= fast (high energy)
i	= ions
n	= neutrals
r	= radial direction
s	= slow (low energy)
x	= axial direction

Superscript

+	= ion, either singly or doubly charged
---	--

Introduction

WITH increased commercial applications of satellites, there is a need for onboard thrusters with relatively long lifetimes. As with other electric propulsion devices, Hall thrusters offer a high specific impulse that is well suited for satellite station-keeping, repositioning, and orbit transfer. The stationary plasma thruster (SPT) variety has been used for many years. Xenon gas is currently the propellant of choice for such devices because it is an inert gas with a

relatively low ionization potential. There is concern, however, about contamination of the satellite surface caused by the plasma in the plume. The charge-exchange plasma, created by collisions between ions and nonionized propellant in which electrons are transferred, is of particular concern. The charge-exchange ions have much lower velocities than the propellant ions; therefore, they are more influenced by the self-consistent electric fields. These fields may cause them to interact with spacecraft surfaces. The charged particles may impact solar arrays or interfere with transmissions from the satellite. Therefore, it is important to understand in detail the dynamics of the plume.

Computational modeling allows the dynamics of the plume and interaction with its environment to be examined without any influences of experimental facilities. The ability to simulate the plumes of these devices allows a wider variety of operating conditions to be tested than would be feasible in a laboratory. Many test chambers can be maintained at fractions of millipascals. However, the operating conditions of these devices give relatively low densities, and thus interactions between the plasma and the background gas are to be expected. Also, the walls of the chamber may influence the plasma. However, computer codes must rely on experimental data for validation. The goal of the present study is to assess the ability to simulate these plumes accurately.

To accomplish this task, a computer code that combines the direct simulation Monte Carlo¹ (DSMC) and the particle-in-cell² (PIC) techniques is being developed to understand in detail the plasma behavior of the plumes of Hall thrusters. The PIC method determines the trajectories of charged particles as predicted by imposed and self-consistent electric fields. The DSMC method is used to simulate the collisional effects in the flowfield. Both charge-exchange and momentum-transfer collisions are modeled. Ions and neutral atoms from the thruster and background atoms are simulated. The code has previously been verified for an ion thruster³ and is being applied to Hall thrusters in the current study. The plumes of these two types of thrusters are similar. The main differences in modeling are in the geometry and the ratio of neutral atoms to ions. Numerical improvements to this earlier version of the code are discussed in the next section.

Because electric propulsion devices such as ion thrusters, arc jets, and Hall thrusters inherently involve charged propellant, the PIC technique is well suited to simulate their plumes. Roy⁴ developed a code for modeling ion thrusters. Wang et al.⁵ have also modeled ion thrusters. Previous work by Oh and Hastings^{6,7} modeled SPT plumes using a PIC-DSMC code. In contrast to the work presented in Refs. 4 and 5, the neutrals are also tracked in the present study, and charge-exchange ions are generated directly from collisions

Received 8 January 1999; revision received 20 August 1999; accepted for publication 15 September 1999. Copyright © 1999 by the American Institute of Aeronautics and Astronautics, Inc. All rights reserved.

*Graduate Student, Mechanical and Aerospace Engineering. Student Member AIAA.

[†]Associate Professor, Mechanical and Aerospace Engineering. Senior Member AIAA.

[‡]Postdoctoral Research Associate, Mechanical and Aerospace Engineering.

between ions and neutrals. The underlying code (MONACO⁸) is a parallel DSMC code to which PIC routines are added. Extensive experimental data have been obtained for the SPT-100 thruster considered in the present study.⁹⁻¹⁴ Measurements of current density and ion velocity were reported in Refs. 10 and 11. Recently, measurements of ion velocity, ion density, heat flux, neutral flux, and plasma potential were obtained.^{12,13} (The reader is also referred to a private communication by C. Marrese and A. Gallimore, University of Michigan, May 1999.) The present study relies on these new data to perform the most comprehensive comparisons between experimental and computational work thus far.

The following subsections describe the assumptions and the numerical approach to the modeling, including a brief explanation of the numerical techniques used. The various simulations are described, followed by a discussion of the results and some conclusions.

Physical Modeling

The plume is comprised of propellant ions, charge-exchange ions, neutral atoms from the thruster, electrons, and the background gas of the experimental facility. The interactions of these species as well as the influence of the electric and magnetic fields are the important modeling issues. The approach to this modeling is outlined in the following paragraphs.

Although utilization efficiencies are high for Hall thrusters, the nonionized propellant accounts for about 50% of the density at the exit. The neutral density is substantially higher when the cathode flow is included. The neutrals may undergo collisions with the ions. Many of these collisions are charge-exchange reactions, where an electron is transferred from a neutral at a relatively low velocity to a high-energy ion. The probability of such a collision is a function of relative velocity and is modeled using the cross section given by Rapp and Francis.¹⁵ This process creates the charge-exchange ions already mentioned. At the thruster exit the nonionized propellant is modeled at sonic conditions based on a temperature of 1000 K. These assumptions yield a neutral velocity of 325 m/s, which agrees well with experiments with a similar Hall thruster.¹⁶ The sonic assumption has been shown to lead to good agreement with experiments of neutral xenon flow.¹⁷

The background gas of laboratory facilities may interact with the propellant during experiments. Although the experiments considered here were conducted with a back pressure of 6 mPa, at room temperature this gives a density on the order of the thruster exit neutral density. The background gas is assumed to be composed entirely of xenon neutrals at 300 K and to be uniform. Collisions with the species that originated from the thruster are simulated, but the background particles are not tracked by the code. Instead, temporary particles are created in each cell with velocities chosen from a Maxwellian distribution and are paired for possible collisions with the species from the thruster. These may be either momentum transfer or charge-exchange reactions. At distances of more than a few centimeters from the exit plane, the background neutrals become the dominant source of charge-exchange ion production. As with the ion thruster plume considered in a previous study,³ the changes to the neutral distribution function would be due to the fast atoms whose density would be at least three orders of magnitude lower than the bulk density. Thus, it is reasonable to assume that the background gas is unchanged with collisions, and it is unnecessary to use computational time and memory on them.

As with the previous study,³ the ions are tracked, but the electrons are not. Instead, the electron behavior is given by a balance of the electrostatic force and the pressure gradient. Mathematically, this is

$$n_e e E = -\nabla p$$

The balance is necessary to prevent the electrons from leaving a region en masse, which would leave behind a large charge imbalance. This equation comes from the electron momentum equation and neglects the collision term and the magnetic field. For the densities and temperatures of the plasma typical of the plumes of Hall thrusters, the ion-electron collision term is negligible. The ratio of the collision frequency to the plasma frequency is much less than 1. The magnetic field term is generally neglected.^{3,4,6} This appears to be

a reasonable estimate for the far field. Further assuming isothermal conditions yields the familiar Boltzmann relation

$$n_e = n_{ref} \exp(e\phi/kT_e)$$

However, the near field in the plumes of Hall thrusters has variations in the electron temperature. The effects of including this variation are considered in the present study. For simplicity, the potential is not calculated in the simulations. Instead, the electric field in the axial and radial direction are calculated directly. Assuming adiabatic conditions, this becomes

$$E_{x,r} = -\frac{kT_e}{e} \frac{d \ln(n_e)}{d(x,r)} - \frac{k}{e} \frac{dT_e}{d(x,r)}$$

An electron temperature is imposed in the domain based on measurements taken by Kim et al.¹⁵ The electrons are assumed to act as an expanding fluid at isentropic conditions. Their density decays as r^{-2} and the temperature scales with $n_e^{\gamma-1}$. Constants are chosen to closely match the measurements of Kim. A comparison in Fig. 1 indicates the good agreement obtained with this approach. A far-field temperature is set for the simulations as well. Simulations are run using both models to determine the effects on the flowfield.

The difference in magnitudes of the ion and electron velocities makes it difficult to also track the electrons in the simulation. By assuming that the plasma is quasineutral ($n_i \approx n_e$), the ion density can be used to find the potential. Both singly and doubly charged propellant ions as well as the charge-exchange ions are included in the simulations. Various ion inlet conditions are used for these simulations to determine whether the comparisons with experimental data are sensitive to the ion profile at the thruster exit.

Figure 2 illustrates the computational domain used for most of the simulations. The domain is assumed to be axisymmetric about the thruster centerline. The main three-dimensional effects would come from the neutralizing cathode. The flow through the cathode is

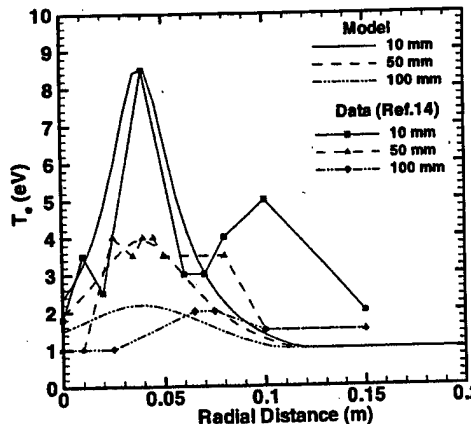


Fig. 1 Comparison of analytical electron temperature to measurements by Kim.¹⁴

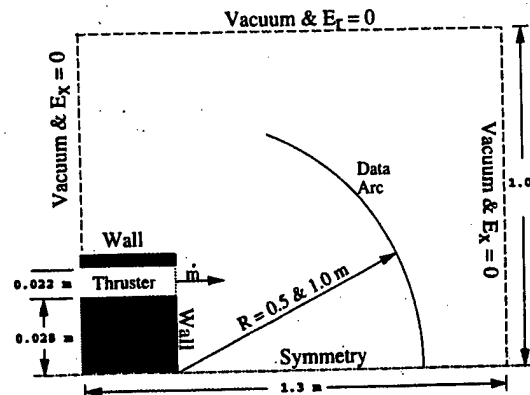


Fig. 2 Computational domain.

assumed to exit from the thruster as neutral xenon atoms. The radial electric field is set to zero on the centerline to satisfy symmetry, but axial variations in potential are permitted. The boundary at the maximum radial position of the domain has the same conditions. The two axial boundaries permit only radial variations in potential. For an adequately large domain the variations at the boundaries would be negligible. Particles that reach boundaries other than the symmetry line leave the simulation. The geometry below the exit plane is simplified. A wall at ground potential is assumed to extend from this exit to the centerline. When an ion strikes a wall, it is neutralized. Thus the assumption is made that an electron strikes the wall as well to maintain quasi-neutrality. The thruster wall boundary condition has little effect on the flow values compared in the results section.

Larger simulations include the full geometry of the experimental facility used at the University of Michigan as the computational domain to better represent the experimental conditions¹³ in the simulations. This domain has a length of 9 m and a radius of 3 m. The walls are assumed to be at ground potential. Particles that reach the walls are removed because the background routine already maintains the facility background pressure. Again the flow is assumed to be symmetric about the thruster centerline.

Computational Modeling

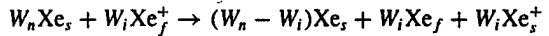
Because both the DSMC and PIC numerical methods rely on particles that represent real molecules, it is desirable to have enough particles to represent the velocity distribution adequately. The following techniques permit larger simulations than would otherwise be feasible.

The underlying DSMC code⁸ is parallelized to run on the IBM SP/SP2 architecture. The computational cells are divided among the processors such that each processor maintains its own collection of neighboring cells. Parallel PIC codes also partition by blocks of cells.¹⁸ However, in the present implementation separate grids are maintained by the two algorithms. The data structures are defined such that the particles are associated with the DSMC grid. These particles are then implicitly mapped to the PIC nodes. For these reasons the PIC algorithm can be run in parallel by a simple tree sum of the charge density at the nodes. The overhead in this method is that each processor has a copy of the entire PIC grid and must calculate the electric field for the entire domain. However, these physical models only require a central differencing scheme for calculating the electric field. By making this simple change to the PIC part of the code, advantage is taken of the underlying parallelization of the DSMC code. For completeness, one time step of the algorithm is shown in Fig. 3.

The behavior of the ions is of primary interest. A sufficient number of ion particles are needed in each cell to represent the ion density for the PIC method without introducing artificial gradients. Therefore, to increase the ion particle count without creating an overabun-

dance of neutrals, a particle weighting scheme is used. The method outlined by Bird for species weighting only conserves momentum and energy on the average, not in each collision.¹ This approach is not conducive to flows with few collisions. A method developed by Boyd¹⁹ splits the particle with the larger weight into two parts. One of these has its momentum changed according to the collision dynamics, and the two parts are recombined afterwards. However, for collision pairs with vastly different velocities, this technique fails to represent the velocity distribution of the species with the larger weight. Charge-exchange reactions commonly involve collision pairs of this type. For this reason a new particle weighting scheme is used for the charge-exchange reactions, whereas Boyd's scheme is used for momentum transfer.

The present scheme is generalized for ion-neutral collisions regardless of which particle has the larger weight, but in these cases the neutral either has an equal or larger weight. The reaction can be described by the following equation:



This scheme has the drawback that a third particle is created in each charge-exchange reaction. However, the mean free path is large enough (≈ 1.2 m at the thruster exit) that this is not a concern. Physically, this shows that only W_i of the W_n molecules undergo a collision and the others are unchanged. This leaves a distribution of $W_n - W_i$ molecules at the same velocity and the other W_i with a much higher velocity. If these two particles were instead recombined using Boyd's scheme, W_n molecules would have a velocity between the extremes that none of these molecules physically would have.

Most of the simulations employ 700,000–800,000 particles in 1600 DSMC cells and 9500 PIC cells on an IBM SP2. These simulations require about 50 CPU h distributed over four processors because the charge-exchange ion timescale is large compared to the propellant ions. Parallel efficiency ranged from 80 to 90%. The fluctuations are caused by the particle weighting scheme. Periodically, a load-balancing routine is used to distribute the particles more evenly among the processors.

Flow Conditions

The nominal operating conditions given in the experiments considered are a current of 4.5 A, a discharge voltage of 300 V, a total flow rate of 5.2–5.4 mg/s with 7% cathode split, and a facility back-pressure of 6 mPa. An ion temperature of 4 eV is assumed at the exit based on Ref. 11 for most of the cases and is compared with a 0.4 eV case (labeled case 3 in the figures). The electron temperature is assumed to be 3 eV based on Ref. 9 and is used to obtain the potential from the Boltzmann relation. These parameters define the input values, but it is necessary to separate them into densities and velocities for each species. The fraction of doubly charged ions is estimated as 25% by Manzella and Sankovic¹⁰ for an SPT-100. This value along with the thruster's efficiency and the assumptions about the neutrals allows exit plane properties for each species to be determined.

The efficiency obtainable at nominal conditions is approximately 0.5 for the SPT-100 Hall thruster.²⁰ A value of 0.54 is chosen for this investigation, which gives an ion velocity close to King's measurements.^{12,13} The ions leave the thruster with a radial component to their velocity.¹¹ Oh and Hastings inverted an analytic function to choose a divergence angle for each particle.⁷ The present study simplifies this process by assuming the divergence angle varies linearly with radial distance from the center of the annulus ring. A maximum of 10 deg is used in one case and 20 deg in another. A uniform ion velocity (0 m/s radial velocity) case is also considered for comparison with current density and heat flux measurements. Each generated ion is chosen from a Maxwellian distribution with the specified average velocity. These velocity profiles are combined with a uniform ion density. See Table 1 for a list of thruster exit conditions used for the sensitivity study.

Table 2 shows the input conditions for examining the effects of a varying electron temperature. The main difference from the other input conditions is that these cases have only 10% of the propellant ions assumed to be doubly charged,¹³ but this negligibly affects

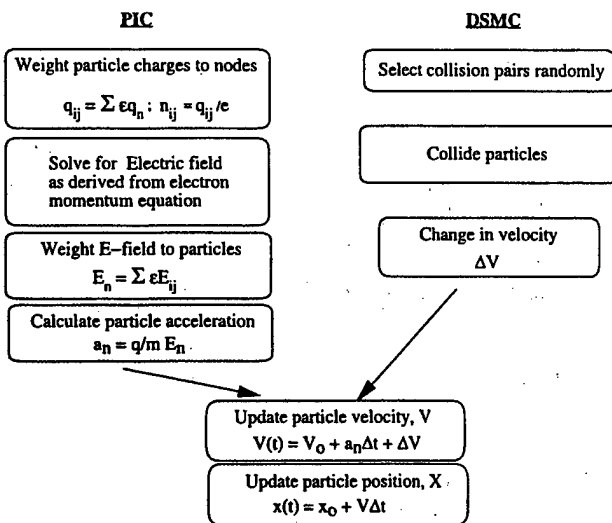


Fig. 3 One time step of the DSMC-PIC algorithm.

Table 1 Ion conditions at thruster exit for sensitivity study

Case	Speed, km/s	Velocity variation	Temperature, eV
1	17.6	$f(r)$: 10 deg	4
2	17.8	$f(r)$: 20 deg	4
3	17.6	$f(r)$: 10 deg	0.4
4	17.5	Uniform	4

Table 2 Input conditions for modeling study

Case	T_e , eV	T_e profile	$n_{e\infty}$, m ⁻³
Ref*	3.0	Constant	6.5e15
VT 1	1.0	Varying	6.5e15
VT 2	2.0	Varying	6.5e15
VT 3*	2.0	Varying	1.3e15

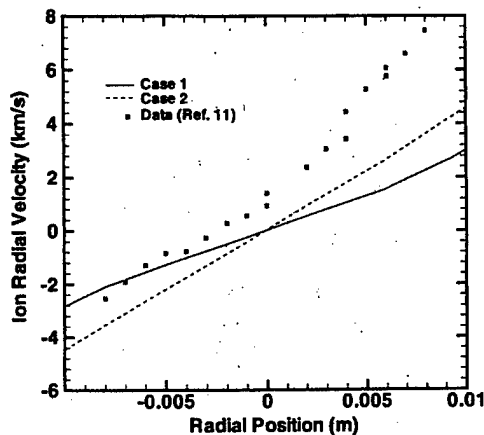


Fig. 4 Comparisons of ion radial velocity at an axial distance of 11 mm.

aggregate ion properties in the plume. The value for reference electron number density determines the magnitude of the potential, but has little effect on the differences in the potential. The value of the electron temperature for the variable electron temperature cases represents the far-field value imposed. The cases marked with asterisks include a full chamber geometry simulation as well as a smaller domain one.

Results

Measurements of radial velocity by Manzella¹¹ indicate an almost linear variation with radial position 11 mm from the thruster exit. A comparison of the simulations with this data is shown in Fig. 4. The simulations also give an almost linear variation that is reasonably close to the data at this axial location. There are significant discrepancies between simulation and data. Neither case reproduces the asymmetry found experimentally because it was not included in the thruster exit plane profile for this investigation.

Comparisons of current density for various simulations with experiments are presented at two different radial locations in Figs. 5–7. The base case (case 1) shown in Fig. 5 agrees well with King's experiment.¹² The comparisons in Figs. 6 and 7 indicate the insensitivity of the computed current density to the variations in inlet ion profiles. The variations are more pronounced close to the centerline; however, each case is within a factor of about two of the data. Comparing cases 1, 2, and 4 indicates the significance of the divergence angle. Clearly, the higher angle leads to a lower peak value at these radial distances. Experiments show a more defined peak than the simulations. The low ion temperature case (case 3) gives a more defined peak, but an underprediction of current density occurs at higher angles.

In Figs. 8–10 the current density is separated into density and velocity components. The velocity comparisons in Figs. 8 and 9 indicate agreement within experimental uncertainty up to about 50 deg. The simulation results only present the average ion velocity

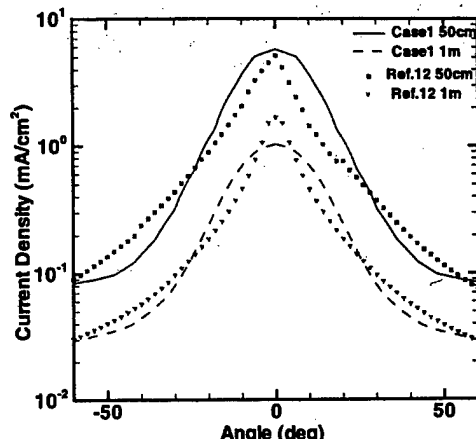


Fig. 5 Comparisons of current density at radial distances of 50 cm and 1 m.

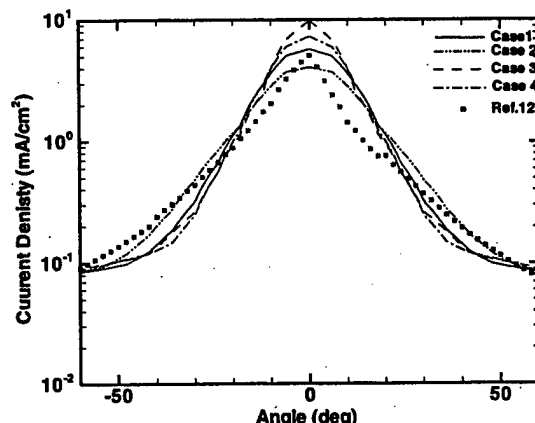


Fig. 6 Comparisons of current density at a radial distance of 50 cm.

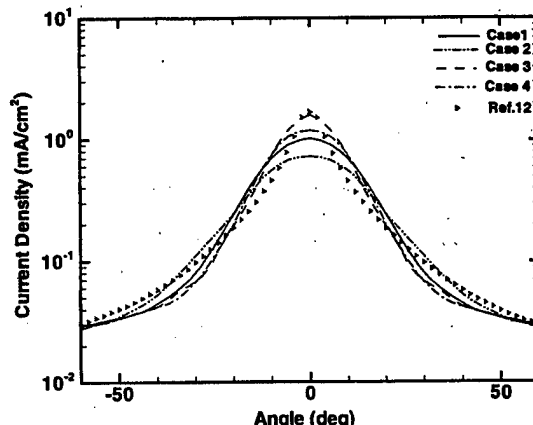


Fig. 7 Comparisons of current density at a radial distance of 1 m.

of the propellant ions, neglecting the charge-exchange ions. The experimental data were obtained from a retarding potential analyzer (RPA).¹³ Numerical differentiation of the current vs voltage data approximates the derivative of this curve, which is proportional to the energy-per-charge distribution function. For singly charged ions of uniform mass, the energy distribution function also represents the velocity distribution function. By normalizing and numerically integrating this velocity distribution function, the average velocity is obtained. This process is likely to minimize the effects of the charge-exchange ions because they only contribute to the current measurements at low voltages. Also, the current scales with the flux of the charge-exchange ions. Thus, the density that is needed to obtain the actual contribution of the charge-exchange ions to the average velocity may be obscured. Therefore, comparing the average

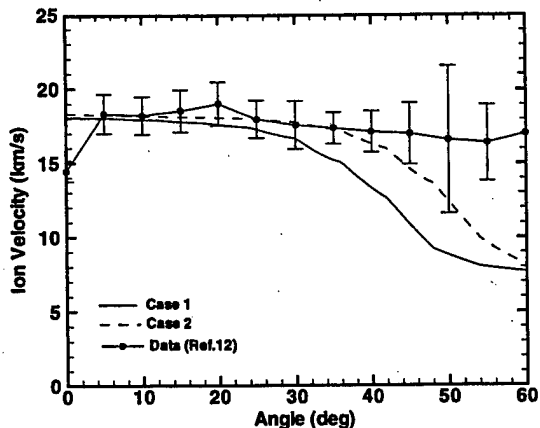


Fig. 8 Comparisons of average ion velocity at a radial distance of 50 cm.

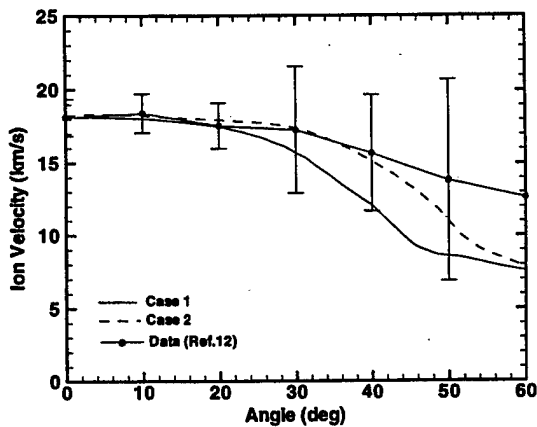


Fig. 9 Comparisons of average ion velocity at a radial distance of 1 m.

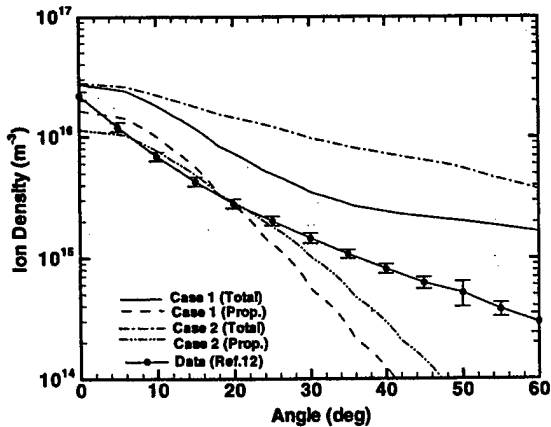


Fig. 10 Comparisons of ion density at a radial distance of 50 cm.

ion velocity of only the propellant ions from the simulation with the experimental measurements is reasonable. The agreement is encouraging. The ion velocity and current density are used to obtain the experimental number density shown in Fig. 10. The simulations allow the ion density to be given directly. Both total density and the propellant ion density of the simulations are shown in Fig. 10. The propellant ion density agrees well at low angles, but it is too low at higher angles where the charge-exchange ions represent a higher fraction. The profile of the total density for case 1 compares favorably with the experiment, but the magnitude is too high. Following the same reasoning as described earlier, the measured ion density should be between the total and propellant densities from the simulation. In contrast to the ion velocity comparisons in Figs. 8 and 9, case 2 does not represent the ion density as well as case 1.

Heat flux measurements were obtained by a heat flux probe consisting of two Schmidt-Boelter thermophile transducers.¹³ The probe was biased to ground potential, which was between 5 and 8 V below the plasma potential, to eliminate electron current heating. Thus, the measured heat flux includes both neutrals and ions. The simulations give the contributions of the ions and the propellant neutrals. The background neutrals contribution is negligible. It is estimated to be on the order of 1 W/m^2 . In Figs. 11–13 comparisons of the simulations with heat flux measurements are shown. There is agreement near the thruster centerline at 50 cm. At 1 m the simulated heat flux is within a factor of three of the measurements. At large angles from the centerline, where charge-exchange ions dominate, there is an underprediction by two orders of magnitude at both locations. The charge-exchange ions have much lower velocities than the propellant ions, and the heat flux scales with velocity

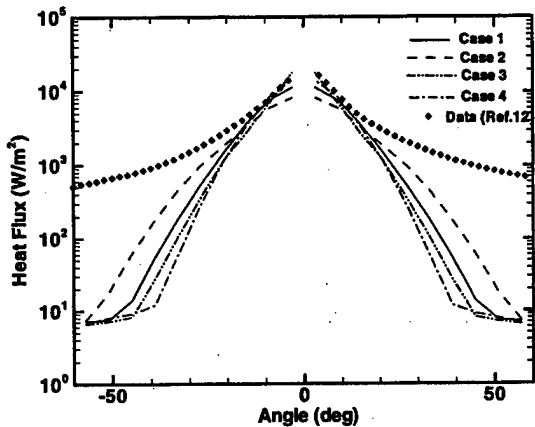


Fig. 11 Comparisons of heat flux at a radial distance of 50 cm.

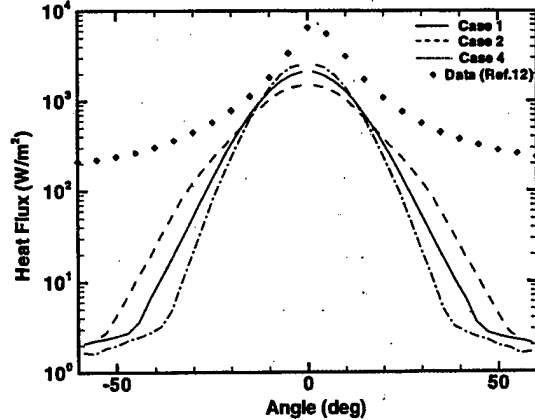


Fig. 12 Comparisons of heat flux at a radial distance of 1 m.

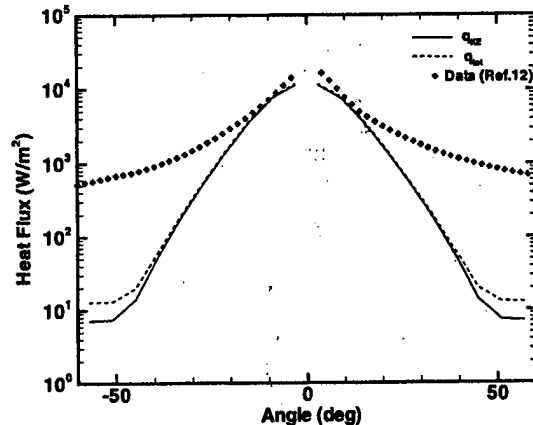


Fig. 13 Comparisons of total heat flux at a radial distance of 50 cm.

Table 3 Integrated heat flux at various radial locations

Case	50 cm, W	1 m, W
King	1692	2339
1	630.0	449.4
2	637.8	460.0
3	609.6	410.1
4	618.3	424.8
Ref	652.5	454.9
VT 1	678.0	468.6
VT 2	678.5	472.6
FG VT	680.3	478.3

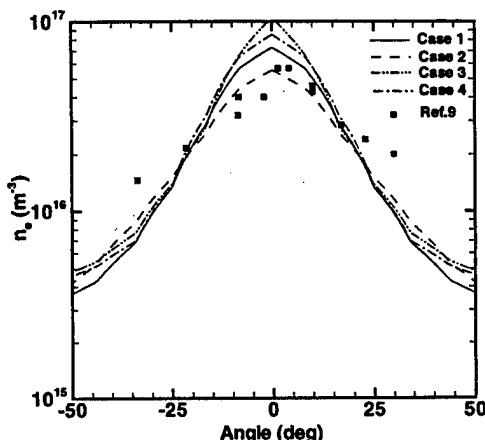


Fig. 14 Comparisons of electron density with measurements by Myers⁹ at a radial distance of 31 cm.

cubed. The spreading of the propellant ions does not improve the agreement at the higher angles significantly, and it leads to poorer agreement near the centerline (Figs. 11 and 12). As with the ion density comparisons, a divergence angle ranging from -20 to 20 deg does not lead to as good agreement as the other cases. The ion temperature has a surprisingly small effect on the heat flux (Fig. 11). The ion temperature affects the spreading of the beam without altering the magnitude of the mean velocity. The higher temperature allows more spreading. The heat flux at higher angles should increase with ion temperature because its magnitude varies as velocity cubed. To estimate the effect on the ions of biasing the probe, an energy of 8 eV is added per ion to the heat flux calculations and is labeled q_{tot} in Fig. 13. Clearly, it is only significant at the larger angles, but it does not make a substantial difference. Upon integrating the heat flux from the experiments, it is found that this heat transfer rate is greater than the power put into the system. Integrated values for the heat flux are shown in Table 3. The electrical power is only 1350 W. The simulations give values indicative of the measured efficiencies ($\approx 50\%$) at a radial distance of 50 cm. By 1 m collisions with the background neutrals have decreased the energy of the ion flow. The simulations, which include a varying electron temperature model, are also included in the table, but plots of the heat flux show only moderate differences from the reference case.

Calculated values for electron density are compared with measurements by Myers and Manzella⁹ at a radial distance of 31 cm in Fig. 14. Cases 1 and 2 show the best agreement. The other cases have inlet conditions that lead to less spreading of the ions. The electron densities from the other set of test cases are shown in Fig. 15. Including a varying electron temperature affects the spreading of the ions. The radial electric field is larger than it would be without a temperature gradient. The case labeled "Ref" is nearly identical to case 1. It is clear from Fig. 15 that the case labeled "VT 3" agrees best with the measurements.

Comparisons with measurements of current density in the plume near field by Kim¹⁴ are shown in Figs. 16 and 17 at three axial locations. At an axial distance of 10 mm, the agreement is reasonable regardless of varying the electron temperature. However, by 100 mm the effects of this temperature gradient are more apparent. The ion

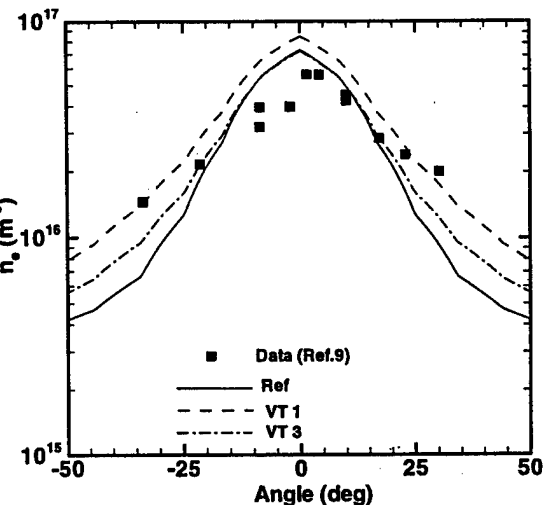


Fig. 15 Comparisons of electron density with measurements by Myers⁹ at a radial distance of 31 cm.

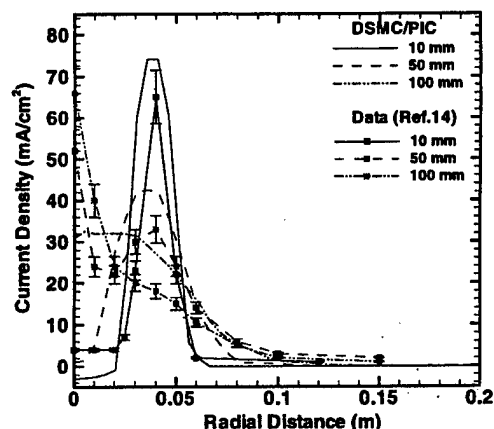


Fig. 16 Comparisons of current density from reference case with measurements by Kim.¹⁴

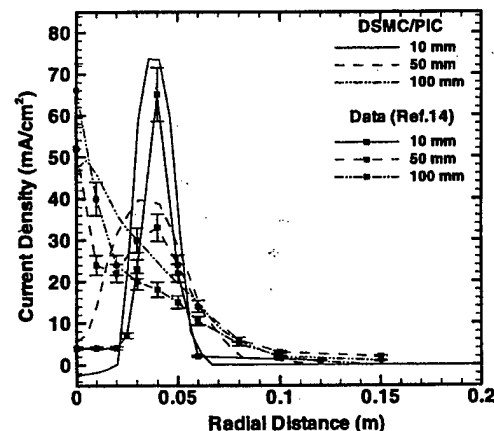


Fig. 17 Comparisons of current density from variable electron temperature case with measurements by Kim.¹⁴

beam reaches the axis more quickly than is predicted by the reference case. The variable electron temperature case more closely matches the shape of the measurements at 100 mm than the reference case. Its peak is about 50% higher than that of the reference case. Even by 50 mm the current density is higher at the axis for a varying electron temperature. For these near-field comparisons there is negligible difference between the different variable electron temperature cases; therefore, only the first is shown. Integrated values are compared in Table 4. At 10 and 100 mm, varying the electron temperature gives only a 4% difference in integrated current.

Table 4 Integrated current at various axial locations

Case	10 mm	25 mm	50 mm	100 mm
Kim	3.97 A	4.92 A	4.95 A	4.51 A
Ref	4.04 A	—	4.09 A	4.19 A
VT 1	4.14 A	—	4.24 A	4.33 A
VT 3	4.13 A	—	4.22 A	4.32 A

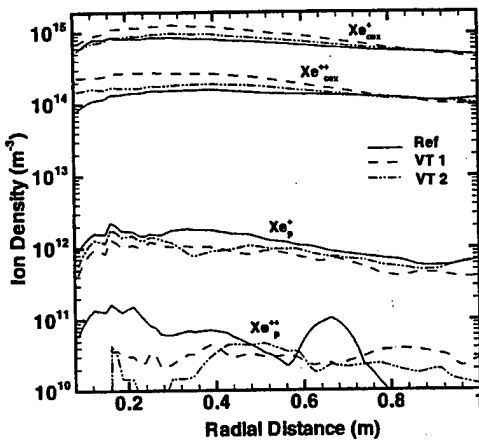


Fig. 18 Comparisons of ion density for the various simulations at an axial distance 4 cm behind the thruster.

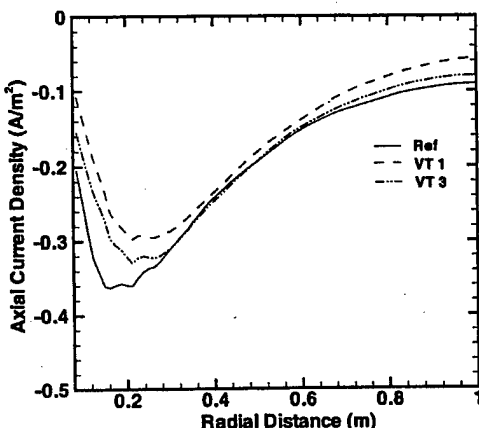


Fig. 19 Comparisons of axial current density for the various simulations at an axial distance 4 cm behind the thruster.

For contamination concerns the backflow and far-field regions are more significant than the near field. The next few figures compare the reference case with the variable electron temperature cases. Figure 18 shows the densities of the various ions 4 cm behind the thruster. Clearly, the charge-exchange ions are most dominant. This is also true well above the thruster in the radial direction because the propellant ions are predominantly axially directed. Comparisons of the charge-exchange ions both behind the thruster and above it for the various cases indicate the significance of the magnitude of the far-field electron temperature. More importantly, the current density shows differences at these locations (Figs. 19 and 20). Behind the thruster the reference case has a magnitude that is a factor of two higher than the $T_e = 1$ eV case near the thruster and 50% higher near the top of the domain. The results are similar at 70 cm above the thruster as well in both the axial and radial directions.

Simulations, which include the full vacuum chamber geometry, allow comparison with experimental data at large angles in the backflow region. The current density from the full geometry cases are compared with measurements by King¹³ at a radius of 50 cm and 1 m in Fig. 21. Even at large angles behind the thruster, good agreement is obtained for both models. The relative insensitivity of the current density to the varying electron temperature coupled with the differences in electron number density suggests that the far-field electron temperature is important.

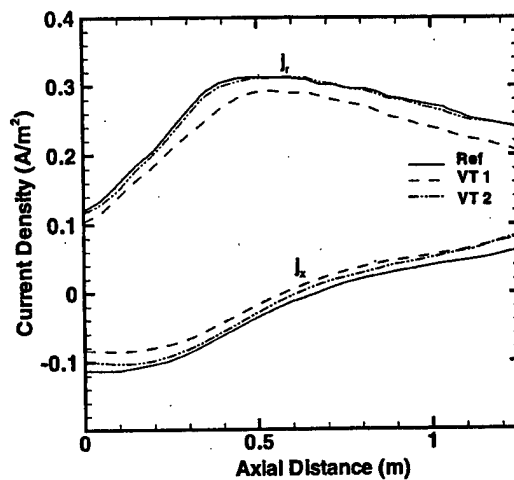


Fig. 20 Comparisons of current density for the various simulations at a radial distance 0.7 m above the thruster.

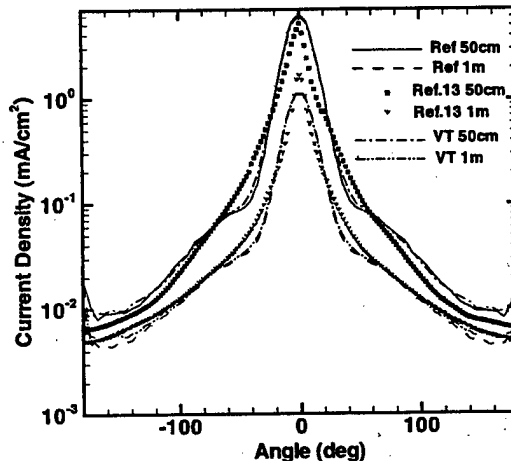
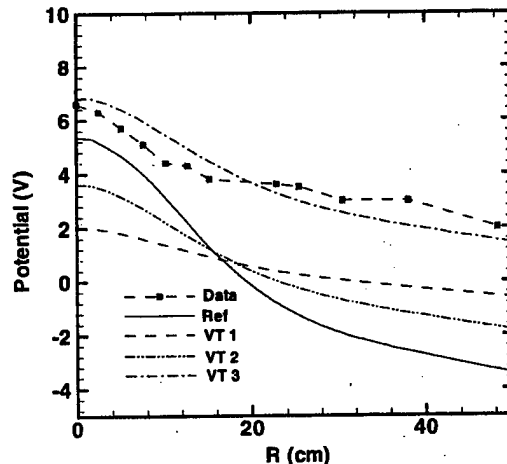
Fig. 21 Comparisons of current density with measurements by King.¹³

Fig. 22 Comparisons of potential with measurements by Marrese (from private communication with A. Gallimore) at an axial distance of 48 cm.

The plasma potential is compared with measurements taken by Marrese and Gallimore (C. Marrese and A. Gallimore, University of Michigan, May 1999, private communication) at an axial distance of 48 cm in Fig. 22. In the simulations the potential drops below zero because of the choice of the reference electron density used in inverting the Boltzmann relation. The experimental measurements here and by King and Gallimore¹³ (in Fig. 23) do not become negative. The third variable electron temperature simulation is shown, which uses a lower value for the reference number density based on Marrese's measurements. This value also agrees with the far-field

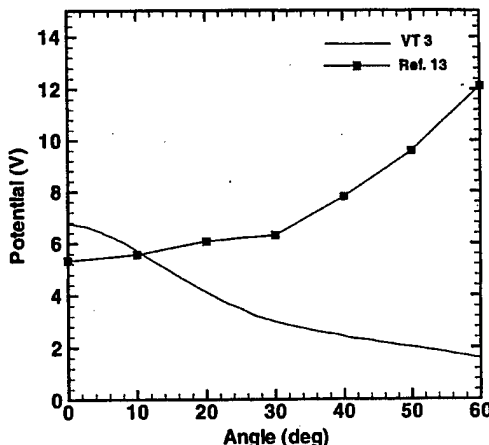


Fig. 23 Comparisons of plasma potential with measurements by King¹³ at a radial distance of 50 cm.

electron density of the simulations. This simulation matches Marrese's data well. The first two variable electron temperature cases have the same shape as Marrese's data but are negative like the reference case. The agreement with King's data (in Fig. 23) is less encouraging. The shape of the potential profile measured experimentally is explained in Ref. 21 through a detailed analysis of the effect on plasma potential of the magnetic configuration of several different Hall thrusters.

Conclusions

A computer code has been developed for simulating Hall thruster plumes. In this study the focus was on examining the sensitivity of the flowfield to various ion inlet conditions as well as to different models for computing the electric fields based on the electron momentum equation. Simulations were performed for the SPT-100 at nominal operating conditions, and comparisons with measured data were presented for a number of plume properties including current density in the near-field, far-field, and backflow regions, and for electron density, heat flux, and plasma potential.

Numerical issues such as computational time and memory cause restraints on the ability to perform large-scale simulations. A particle weighting scheme was used to allow a sufficient number of ions in the computational domain without an overabundance of neutral particles. This scheme better represents the velocity distribution than a weight-by-species method. The parallel nature of the code allows large-scale simulations. These two numerical techniques offer the capabilities of accurately simulating the physical models.

Calculations of far-field ion properties are affected by variations in the ion inlet profile. However, the comparisons with experimental data show only moderate differences. Each of the various simulations agreed well with experimental measurements of far-field ion current density.

Including a varying electron temperature was found to be significant in the modeling of Hall thruster plumes. The electron temperature gradient significantly affects the near-field of the plume. Simulations incorporating the varying electron temperature model gave better agreement with the near-field current density measurements than those using the isothermal Boltzmann relation. Results suggest that outside of this region the plasma behavior is not dictated by this near-field behavior, but rather by the value of the electron temperature. Thus, the far-field electron temperature is also important. This temperature is likely to be lower than the near-field value. The simulations agreed well with the measurements of electron number density. Agreement with plasma potential was dependent on the value for the reference density used in the physical models.

Simulating the full geometry of the experimental facility is important to consider measurements for code validation of the backflow

region. This can also aid in determining any possible effects from the facility. The simulations were found to represent the current density very well. Even at large angles behind the thruster, good agreement was obtained with experiment.

Acknowledgments

Funding for this research was provided by NASA John H. Glenn Research Center through Grant NAG3-1451 and by the Air Force Office of Scientific Research through Grant F49620-96-1-0091. The authors also wish to thank Lyon B. King for making the experimental data available for comparison.

References

- ¹Bird, G. A., *Molecular Gas Dynamics and the Direct Simulation of Gas Flows*, Oxford Univ. Press, Oxford, 1994.
- ²Birdsall, C. K., and Langdon, A. B., *Plasma Physics via Computer Simulation*, Adam Hilger, Bristol, England, U.K., 1991.
- ³VanGilder, D. B., Font, G. I., and Boyd, I. D., "Hybrid Monte Carlo-Particle-in-Cell Simulation of an Ion Thruster Plume," *Journal of Propulsion and Power*, Vol. 15, No. 4, 1999, pp. 530-538.
- ⁴Roy, R., Samanta, "Numerical Simulation of Ion Thruster Plume Backflow for Spacecraft Contamination Assessment," Ph.D. Dissertation, Dept. of Aeronautics and Astronautics, Massachusetts Inst. of Technology, Cambridge, MA, May 1995.
- ⁵Wang, J., Brophy, J., and Brinza, D., "3-D Simulations of NSTAR Ion Thruster Plasma Environment," AIAA Paper 96-3202, July 1996.
- ⁶Oh, D., and Hastings, D., "Three Dimensional PIC-DSMC Simulations of Hall Thruster Plumes and Analysis for Realistic Spacecraft Configurations," AIAA Paper 96-3299, July 1996.
- ⁷Oh, D., and Hastings, D., "Axisymmetric PIC-DSMC Simulations of SPT Plumes," International Electric Propulsion Conf., Paper 95-160, Sept. 1995.
- ⁸Dietrich, S., and Boyd, I. D., "Scalar and Parallel Optimized Implementation of the Direct Simulation Monte Carlo Method," *Journal of Computational Physics*, Vol. 126, 1996, pp. 228-243.
- ⁹Myers, R. M., and Manzella, D. H., "Stationary Plasma Thruster Plume Characteristics," International Electric Propulsion Conf., Paper 93-096, July 1993.
- ¹⁰Manzella, D. H., and Sankovic, J. M., "Hall Thruster Ion Beam Characterization," AIAA Paper 95-2927, July 1995.
- ¹¹Manzella, D. H., "Stationary Plasma Thruster Ion Velocity Distribution," AIAA Paper 94-3141, Aug. 1994.
- ¹²King, L. B., and Gallimore, A. D., "Ionic and Neutral Particle Transport Property Measurements in the Plume of an SPT-100," AIAA Paper 96-2712, July 1996.
- ¹³King, L. B., "Transport-Property and Mass Spectral Measurements in the Plasma Exhaust Plume of a Hall-Effect Space Propulsion System," Ph.D. Dissertation, Dept. of Aerospace Engineering, Univ. of Michigan, Ann Arbor, MI, May 1998.
- ¹⁴Kim, S., Foster, J. E., and Gallimore, A. D., "Very-Near-Field Plume Study of a 1.35 kW SPT-100," AIAA Paper 96-2972, July 1996.
- ¹⁵Rapp, D., and Francis, W. E., "Charge Exchange Between Gaseous Ions and Atoms," *Journal of Chemical Physics*, Vol. 37, No. 11, 1962, pp. 2631-2645.
- ¹⁶Cedolin, R. J., Hargas, W. A., Jr., Hanson, R. K., and Capelli, M. A., "Laser-Induced Fluorescence Diagnostics for Xenon Hall Thrusters," AIAA Paper 96-2986, July 1996.
- ¹⁷Boyd, I. D., VanGilder, D. B., and Liu, X., "Monte Carlo Simulation of Neutral Xenon Flows of Electric Propulsion Devices," *Journal of Propulsion and Power*, Vol. 14, No. 6, 1998, pp. 1009-1015.
- ¹⁸Roy, R., Samanta, Hastings, D. E., and Taylor, S., "Three-Dimensional Plasma Particle-in-Cell Calculations of Ion Thruster Backflow Contamination," *Journal of Computational Physics*, Vol. 128, 1996, pp. 6-18.
- ¹⁹Boyd, I. D., "Conservative Species Weighting Scheme for the Direct Simulation Monte Carlo Method," *Journal of Thermophysics and Heat Transfer*, Vol. 10, No. 4, 1996, pp. 579-585.
- ²⁰Sankovic, J. M., Hamley, J. A., and Haag, T. W., "Performance Evaluation of the Russian SPT-100 Thruster at NASA LeRC," International Electric Propulsion Conf., Paper 93-094, Sept. 1993.
- ²¹Keidar, M., and Boyd, I. D., "Effects of a Magnetic Field on the Plasma Plume from Hall Thrusters," *Journal of Applied Physics*, Vol. 86, No. 9, 1999, pp. 4786-4791.

R. G. Wilmoth
Associate Editor